ANTHROPOMORPHIC HUMAN CAROTID ULTRASOUND PHANTOM

Caleb Darr

A thesis submitted to the faculty at the University of North Carolina at Chapel Hill in partial fulfillment of the requirements for the degree of Master of Science of Biomedical Engineering in the Joint Department of Biomedical Engineering in the School of Medicine.

Chapel Hill
2022

Approved by:

Caterina Gallippi

Paul A Dayton

Boyce Griffith

ABSTRACT

Caleb Darr: Anthropomorphic Human Carotid Ultrasound Phantom
(Under the direction of Caterina Gallippi)

Vascular hemodynamics and plaque composition are indicators of stroke risk. Previous work indicates that multi-angle Plane Wave (PW) implementation of Acoustic Radiation Force Impulse (ARFI), Log Variance of Acceleration (log(VoA)), and 2-D Vector Doppler (VD) imaging can detect plaque structure and composition. Additional preceding work used Fluid-Structure Interaction (FSI) modeling to simulate blood fluid dynamics to estimate Wall Shear Stress (WSS) for plaque characterization and rupture risk evaluation. Anthropomorphic tissue-mimicking phantoms are constructed to recapitulate WSS measurements in complex human carotid arteries with pronounced plaques. Ultrasound experiments using duel PW Log(VoA) and 2D VD sequences under steady-state flow conditions are compared to the analogous FSI model simulations. The results suggest that thin-walled and wall-less anthropomorphic flow phantoms can be constructed to resemble the FSI model in physical geometry and WSS vessel profiles. These flow phantoms are currently limited to construction challenges.

ACKNOWLEDGEMENTS

I would like to thank my supervisor Dr. Caterina Gallippi for all her help and advice with this MS. I would also like to thank my wife, whose continual support made the accomplishment of this work possible. I also appreciate all the support I received from the rest of my family. Lastly, I thank Keerthi Anand for the mentorship that equipped and encouraged me to conduct this thesis.

TABLE OF CONTENTS

LIST OF FIGURES

LIST OF TABLES

LIST OF ABBREVIATIONS

ARFI	Acoustic Radiation Force Impulse
CAD	Computer-Aided Design
CD	Calcium Deposits
CFD	Computational Fluid Dynamics
ECA	External Carotid Artery
FSI	Fluid-Structure Interaction
ICA	Internal Carotid Artery
IH	Intraplaque Hemorrhage
LRNC	Lipid Rich Necrotic Core
MAD	Mean Absolute Deviation
MRI	Magnetic Resonance Imaging
PLA	Polylactic Acid
PVA	Poly(vinyl alcohol)
RF	Radio Frequency
VoA	Variance of Acceleration
WSS	Wall Shear Stress
μCT	Micro-Computed Tomography

CHAPTER 1: INTRODUCTION

1.1 Atherosclerosis Background

According to the World Stroke Organization, 13.7 million new strokes occur each year, and for individuals over the age of 25, one in four will have a stroke in their lifetime [1]. Strokes can be divided into two major sets: ischemic and hemorrhagic. A hemorrhagic stroke originates within the brain and is caused by blood vessel rupture. The deficiency of oxygen delivery to maintain aerobic metabolism and the release of damage-associated molecular patterns induces a systemic inflammatory responses that eventually lead to widespread brain cell death [2]. An ischemic stroke produces a similar oxygen deficiency within the brain; however, it results from blood vessel obstruction. Whether in the neck or inside the brain, the affected blood flow is restricted by one of the following three mechanisms: clot formation, called thrombosis, transfer of clot to brain after dislocation from vessel wall, called embolism, or narrowing of the vessel flow area or lumen, called stenosis [3]. Of all strokes, 9.5 million are ischemic in origin, where a blockage in an artery reduces the blood supply to the brain, and 2.7 million will result in patient death [1]. A significant contributor to stroke-related morbidity is atherosclerosis.

Atherosclerosis develops most commonly in medium to large arteries such as the carotid vessels and is marked by the accumulation of lipid-laden foam cells leading to a chronic inflammatory response at vulnerable arterial wall locations [4]. These fatty streaks develop fibrous fibroatheromas. Further progression leads to either a stable or unstable plaque. Stability is marked by plaque regression, static state, or retarded development with low lipid content and thick fibrous caps. Conversely,

unstable plaques are characterized by thick lipid cores, regions of intraplaque hemorrhage, and thin fiber caps [4].

Beyond the physical structure, the viscous blood flow across the affected endothelial cells significantly influences plaque formation and rupture risk [5], [6]. The wall shear stress (τ_w) is a tangential stress exerted upon the vessel wall and is a product of the fluid viscosity (μ) and shear rate (dv/dy): $\tau_w = \mu(dv/dy)$ [7], [8]. Healthy physiological time averaged wall shear stress (WSS) is expected to reside between $1.5 - 2.5$ Pa; values above and below this range constitute substandard rates [9]. When WSS falls below 1.5 Pascals a vessel can be characterized as atheroprone; conversely, when the cardiac cycles is at diastole a high WSS indicates a rupture-prone plaque [10]. Hemodynamic deviations resulting in low WSS have shown to negatively affect vessel morphology and biochemical processes in such a way as to promote the evolution of atherosclerosis [11]–[14]. Continued plaque growth resulting in pronounced stenosis of the lumen wall, however, eventually causes supraphysiological WSS. This accelerated blood flow across the fibrous cap increases susceptibility to fissuring or rupture [15]–[17]. These factors, along with structural features such as intraplaque hemorrhages, calcium deposits, and lipid-rich necrotic cores, all influence plaque rupture vulnerability [18], [19]. These rupture risk factors are essential indicators of stroke due to the potential exposure of thrombogenic material that initiates clotting and ensuing acute thrombotic episodes [20].

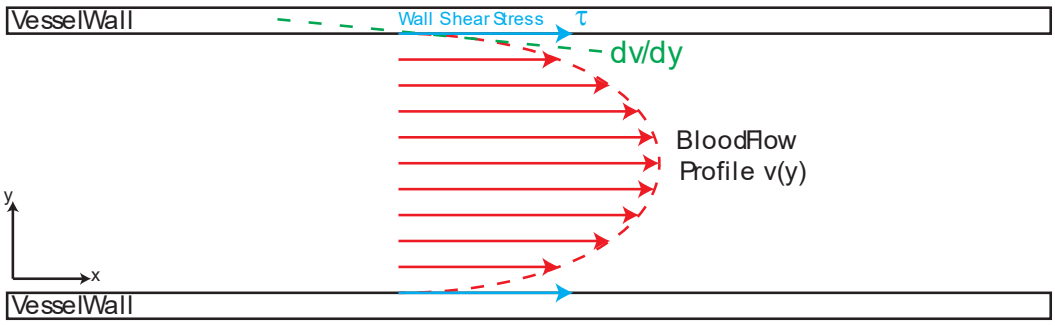

Figure 1: Parabolic flow profile.

1.2 Wall Shear Stress Measurement

A wall shear stress estimation along the vessel geometry can provide insight into the hemodynamic factors influencing a plaque's rupture risk. Although no gold standard has yet been established to estimate human blood flow WSS, numerous methods are available with significant advantages and limitations [21]. Assuming Poiseuille flow, WSS can be calculated by estimating the vessel diameter and maximum blood velocity [22]. This model, however, makes the following assumptions: blood is a Newtonian fluid, the blood flow is laminar and fully developed, the flow does not slip at the vessel boundary, the flow has reached steady-state conditions, the lumen is cylindrical, and the vessel wall is rigid [8]. The only assumption preserved under *in vivo* conditions is the no-slip condition at the vessel wall [7]. The remainder are overcome due to the hemodynamic conditions of physiological flow. For instance, blood is a shear-thinning fluid due to the aggregation and breaking up of red blood cell rouleaux at high strain rates [23]. Furthermore, during a cardiac cycle from systole to diastole, the flow may not be laminar and fully developed and most definitely is not at steady-state flow with perfectly cylindrical and rigid vessel walls [7]. Understanding these considerations, WSS estimation employing the Hagen-Poiseuille equation under pulsatile biological flow, particularly in the vicinity of lumen stenosis and complex plaque geometry, is severely limited [21]. Another ultrasound-based WSS estimation method utilizes intravascular probes. The shear rate is estimated by obtaining the blood velocity profile, and WSS is subsequently calculated. The invasive nature of this procedure is disadvantaged by the disruption of the original flow from the foreign object within the lumen [24].

Alternatively, WSS estimation by magnetic resonance imaging (MRI) is achieved through phase contrast velocity mapping [25]. The velocity profiles are used to derive shear stress values close to the wall; however, due to low spatial resolution, blood flow cannot be estimated closer than approximately one millimeter from the wall. This resolution results in an underestimation of the WSS [26]. Coupling this limitation with the low temporal resolution of MRI, the WSS cannot be calculated

as a function of the cardiac cycle, thus, limiting the modalities' use in plaque rupture characterization [27].

Plane-wave Doppler ultrasound estimates the axial blood flow away from or toward the array. The blood flow velocities and direction can be estimated using the multiangled plane-wave vector doppler sequences developed by Anand et al. [39]. Plane-wave vector doppler algorithms offer a high frame rate method capable of performing WSS estimation throughout the cardiac cycle. Coupling this high temporal resolution with the multiangled plane-wave sequences, an estimation of WSS and plaque composition can be performed by calculating the tissue Log (Variance of Acceleration) [28]. This parameter, in short, estimates the tissue jitter and correlates with tissue-specific characteristics capable of differentiating atherosclerotic plaque morphology [29], [30].

The final approach using computational fluid dynamics (CFD) solves the Navier-Stokes fluid flow equations to estimate WSS given finite volumes or elements of the given geometry [21]. For simple geometries, this method can calculate the WSS using analytical expressions. Similar models have been developed by Anand et al. [39] to simulate the blood flow and calculate the wall shear stress in 3D human plaque computer models. These techniques offer a model capable of validating experiments by other forms of WSS estimation, such as plane-wave Doppler ultrasound. However, it should be noted that currently, these models have difficulty modulating the vessel geometry as a function of the cardiac cycle to simulate wall motion and pulsatile flow [31].

1.3 Validation Standard

As no gold standard has been established for WSS measurement, a multimodal approach must be taken to ensure accurate and reliable estimations [21]. A Fluid-Structure Interaction (FSI) model can simulate arbitrary geometries and calculate the velocity gradient precisely at the vessel wall to produce a WSS estimation. Assuming the FSI model is a viable validation standard, the ultrasound vector Doppler techniques can be scrutinized using the flow phantoms described in this work. The

objective is to develop anthropomorphic phantoms that can be a reliable stand-in for human carotids to assist WSS measurement technology development.

By constructing tissue-mimicking flow phantoms with geometries and material properties matched to those of human carotid arteries with atherosclerotic plaques, ultrasound-based vector Doppler sequences can be used to estimate WSS *in situ*. Using the FSI standard, the developed anthropomorphic flow phantoms can be validated to the simulations. We hypothesize that the development of anthropomorphic tissue-mimicking phantoms can be produced to recapitulate wall shear stress measurements in the complex human carotid arteries with pronounced plaques to enable matched experimental and simulated wall shear stress measurement.

1.4 Flow Phantoms

The need for an anthropomorphic atherosclerotic carotid flow phantom has previously been investigated by several individuals using various mold techniques and tissue-mimicking materials [32]–[34]. A method employed by Dong *et al.* utilizes a simple bifurcated geometry designed in a CAD package with a 3D-printed thin-walled vessel and a water-soluble polyvinyl alcohol filament [32]. This phantom, although simple in construction, lacks any features that would distinguish human carotid arteries. Galluzzo *et al.* and Chee *et al.* improve their anthropomorphic flow phantoms from previous attempts by using a CAD package to design thin-walled vessel geometries resembling typical human carotids with varying levels of stenosis [33], [34]. Although these phantoms appear to have similar geometries, they were not compared to a validating standard to substantiate the ultrasound-based flow measurements and are not designed using actual human geometries.

To further develop novel ultrasound-based atherosclerosis plaque rupture risk assessment, this work hypothesizes that human carotid blood flow hemodynamics can be recapitulated with thin-walled and wall-less anthropomorphic flow phantoms. The exact geometry of human cadaveric

carotids containing atherosclerotic plaque can be modeled by utilizing additive manufacturing techniques combined with injection molding of acoustically appropriate materials.

CHAPTER 2: METHODS

2.1 Cadaveric Carotid Geometry

An initial biological sample must be obtained for model imitation to generate anthropomorphic flow phantoms that accurately reflect human geometry and flow conditions. This sample comes from excised human carotids sourced from the University of North Carolina Autopsy Services within forty-eight hours of death. Approximately five-centimeter sections of the carotid bifurcation with the external carotid artery (ECA) stitched closed are imaged using the ultrasound sequences described in the "Data Acquisition" section below. After baseline ultrasound imaging, the carotids are pressurized to eighty millimeters of mercury to simulate diastolic pressure and placed in a solution of ten percent formalin for twenty-four hours. This process fixes the geometry of the carotid by cross-linking amino groups within the vessel [35].

Figure 2: Left excised human female age 68 carotid (C30)

The fixed cadaveric carotids are imaged using volumetric micro-Computed Tomography (μCT) and exported using the DICOM file type. The imaging files are loaded into Slicer to extract the geometry as stereolithography (.stl) file; however, due to the high resolution of the μCT and uneven tissue surface, the geometry is very noisy with many sharp edges. The geometry is smoothed through triangular reduction using Mesh Mixer, and circular inlet and outlet conditions are added to the ends of the vessel using a CAD package. This process results in a 3D rendering of the intended cadaveric internal carotid artery (ICA) that will be used to develop molds and 3D printed geometries to construct anthropomorphic flow phantoms. Akin to a pipe with both an inside and outside wall, these models embody both the external geometry of the vessel wall and internal contours representing the boundary of the lumen fluid flow area. These models allow for comprehensive modeling of the geometry in question. The excised human carotid used for phantom development in this manuscript is sample C30, a left human carotid artery obtained from a sixty-eight-year-old female.

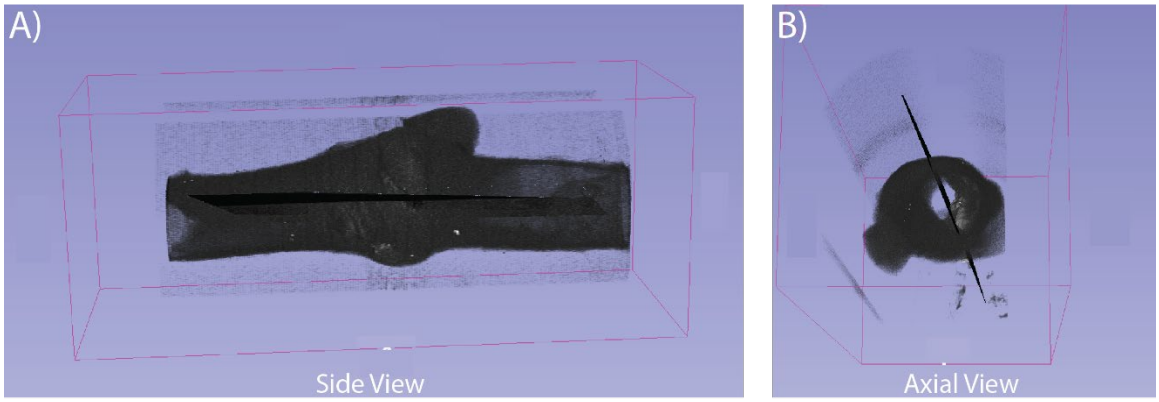

Figure 3: 3D Micro-CT of excised human carotid (C30)
Left Human female age 68 carotid artery. A) Side view of 3D volumetric micro Computed Tomography B) Axial view of the carotid.

2.2 Phantom Construction Methodology

2.2.1 Vessel Geometry Models

Once a 3D model of a carotid artery is developed with interior and exterior geometries, see Figure 4, it must be processed to export the inside and outside geometries separately. A CAD package is used to generate additional extensions on the inlet and outlets of the vessel geometry. Figure 5, panel A) shows the internal geometry and the extensions added on either end. Note the constant diameter of the extensions; this ensures that vessels constructed from the internal geometry will allow blood-mimicking fluid to fully develop upon entering the plaque's geometry. In contrast, Figure 5 panel B) depicts the external geometry where the extensions gradually increase in diameter. This thickening of the vessel wall outside the imaging region allows for increased strength and durability to prevent potential ruptures at the inflow and outflow junctions.

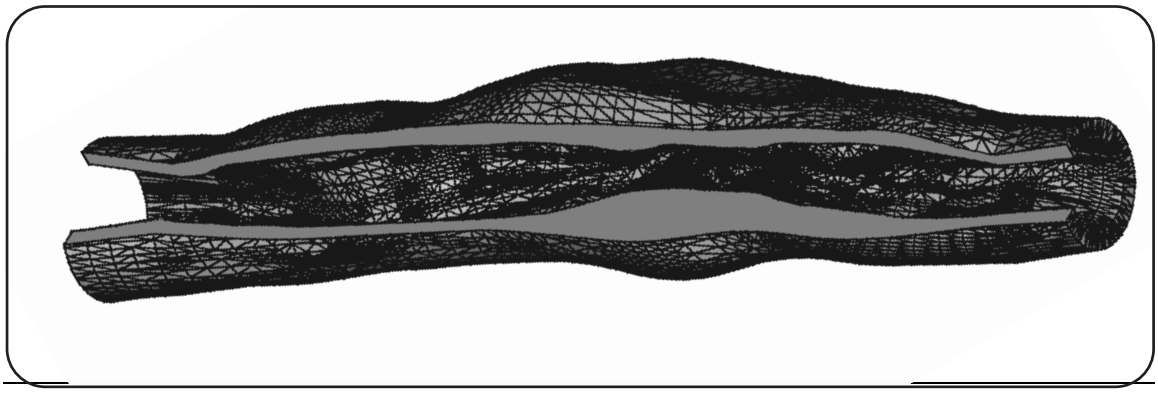

Figure 4: 3D smoothed vessel geometry cross-section of carotid C30.
One-quarter of the vessel is removed to allow inspection of inner and exterior geometries.

The models seen in Figure 5 can be printed using 3D additive manufacturing techniques. The 3D printer used to print the geometries illustrated in Figure 6 is a Prusa i3 MK3S+. The printer is loaded with PLA plastic, configured with a layer slice of 0.1 mm, an infill pattern of gyroid at fifteen percent fill, and support structures added up to the top layer of the print. After the support material is removed upon completion of the print, additional surface smoothing can be achieved using a soldering iron with low heat and light pressure. The result is a smooth finish along the entire length

of the internal and external vessel geometries. These will be used to cast both wall-less and thin-walled vessels to produce two variations of anthropomorphic flow phantoms.

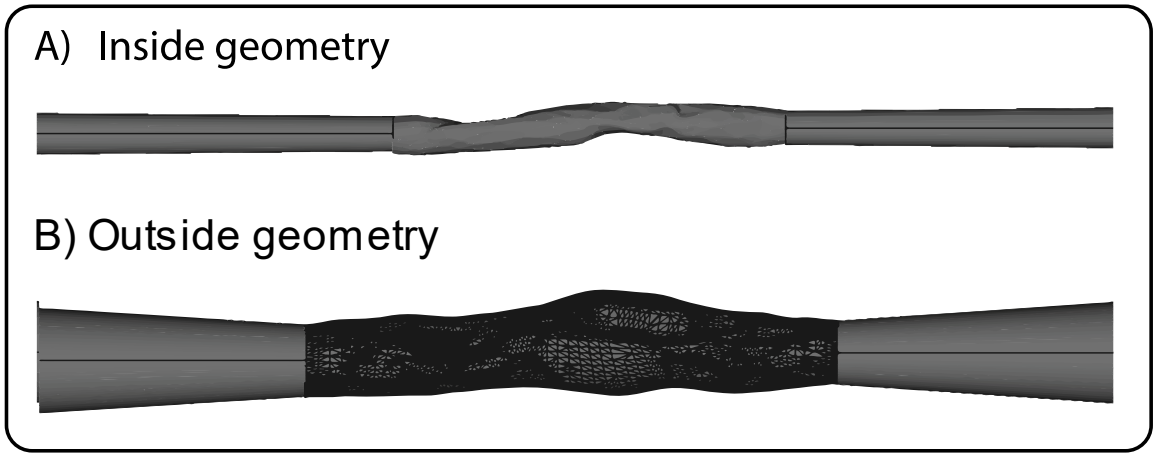

Figure 5: C30 vessel geometry.
Interior vessel geometry of cadaveric carotid C30. B) Exterior vessel geometry of cadaveric carotid C30.

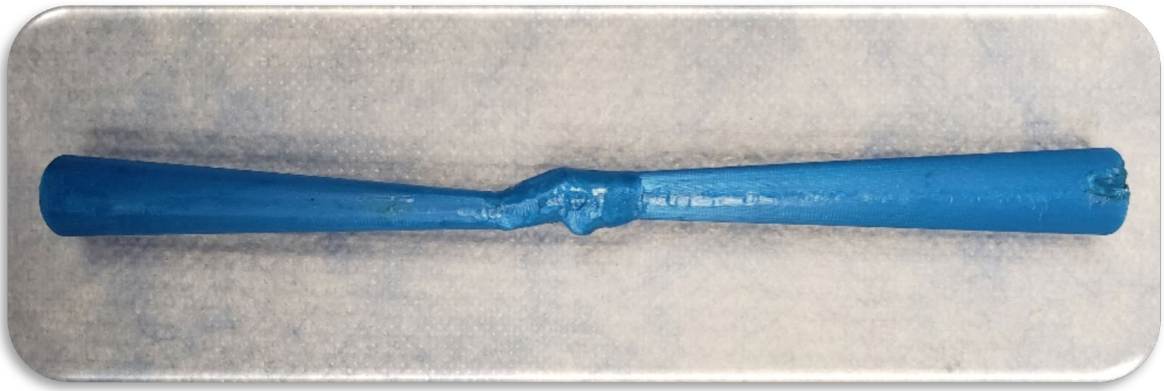

Figure 6: C14 exterior geometry 3D print.

2.2.2 Mold Design

To form a thin-walled vessel, additional processing of the external geometry is required; therefore, a negative relief must be formed to allow for simultaneously casting of the internal and exterior geometries. A clamshell-type mold developed using a CAD package is illustrated in Figure 7. The dimensions are such that the 3D-printed vessel geometries fit within the mold, as illustrated in Figure 7. The key mold design features are highlighted in Figure 8. The mold is designed with two inlet ports to inject casting material from either side. This method allows for the even distribution of

material throughout the transient casting process. Likewise, two mold overflow vents allow air and excess material evacuation. These vents are crucial in ensuring a consistent and defect-free casting. A large rectangular cavity in the center of the mold allows for the accumulation of casting material and will result in a negative relief of the geometry affixed within the two-part mold. One of two features affixes the vessel geometry within the mold at the desired location. The lumen guides suspend the smaller internal geometry at either end of the mold, see item E) of Figure 8, while the lumen coupling wells support the larger exterior vessel geometry, see items A) and B) of Figure 8. Note the singular support at the inlet and triple support for the outlet. This feature ensures the flexibility of the mold to cast both straight vessel geometries, panel A), and bifurcated carotid arteries, panel B) of Figure 9. The final key design element is the mold guides, item D Figure 8. These pin and hole structures on either half ensure the vessel geometries line up each time the mold is clamped together. Additionally, the wide spacing of pins on the inlet and narrow spacing for the outlet ensures the mold cannot be clamped together in a configuration where the vessel geometries are facing opposite directions. These features safeguard from operator error and the generation of faulty phantoms.

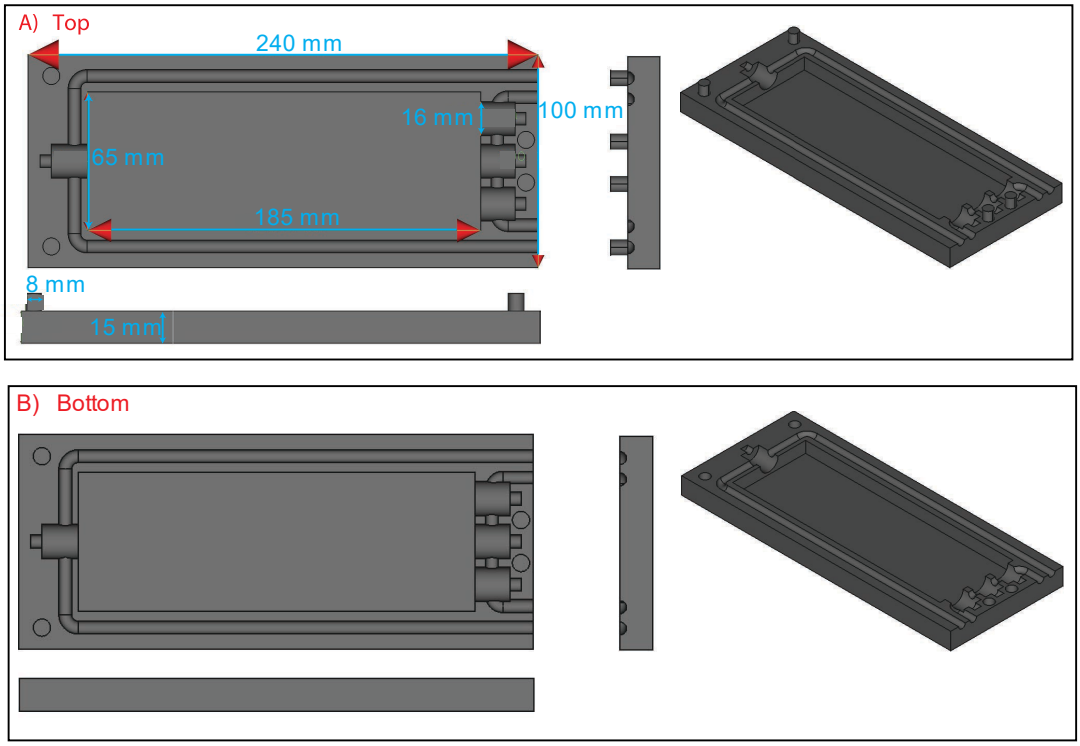

Figure 7: 3D printed molds.
A) The top half of 3D printed mold with protruding mold guides allow proper alignment. Critical dimensions are given in millimeters. ***B)*** *Bottom half of 3D printed mold with receiving mold guides.*

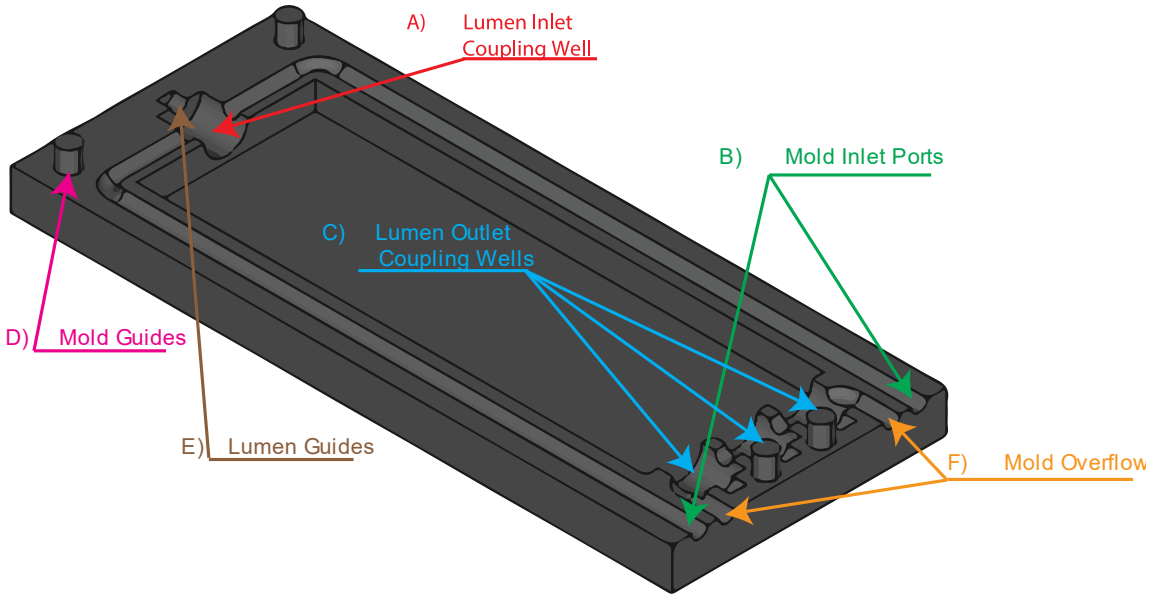

Figure 8: Mold anatomy.
A) Lumen inlet coupling well allows the thin-wall lumen to have a thick-walled inlet to aid in connecting pipe fitting to the lumen. B) Mold inlet ports allow liquid PVA or silicon rubber injection. C) Lumen outlet coupling well allows the thin-wall lumen to have a thick-walled outlet to aid in connecting pipe fitting to the lumen. Note that the three-outlet ports allow straight tube or bifurcation phantom design compatibility. ***D)*** *Mold guides allow for proper alignment of two halves of mold to be correctly lined up for casting.* ***E)*** *Lumen guides allow interior vessel geometry to be suspended properly inside the mold to cast a thin-walled lumen.* ***F)*** *Mold overflow ports allow excess liquid PVA or silicon rubber to vent from the mold and allow air bubbles to escape.*

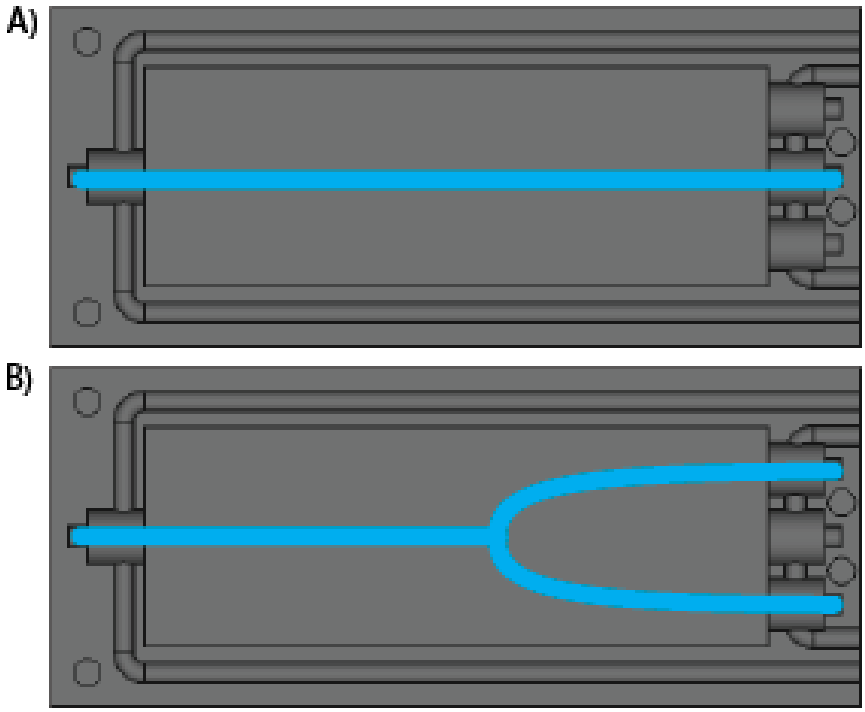

Figure 9: Multiple mold configurations
Straight vessel mold configuration. B) Bifurcation vessel mold configuration

2.2.3 Silicon Casting

In preparation for casting a negative relief of the exterior vessel geometry, a sealant must be applied to the two-part mold. For this purpose, one hundred percent white petrolatum is applied to the touching surfaces of the two halves. To prevent excess petrolatum from interfering with the casting process, the mold must be prestressed, as in Figure 11, to squeeze out the surplus sealant. Upon opening the prestressed mold, the excess petroleum jelly can be removed. This preparation will prevent defects from being introduced by the presence of unwanted sealant. With the mold prepared and the exterior geometry placed within the two halves, see Figure 10 and Figure 12, a silicon rubber and curing agent solution is injected using a fifty-milliliter syringe. A system of bifurcated hoses is utilized to evenly distribute the solution to both mold inlet ports and provide uniform filling. This process is illustrated in Figure 12, and an example is shown in Figure 11.

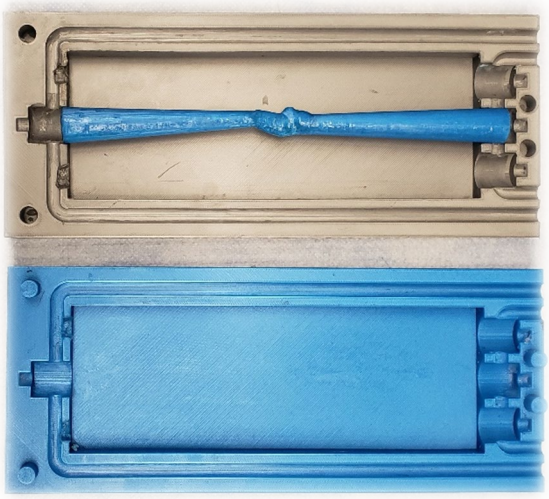

Figure 10: Exterior vessel geometry casting.
Top and bottom halves of mold with exterior vessel geometry of cadaveric carotid C14 preparation for casting negative relief in silicon rubber.

Figure 11: Casting injection configuration.
A 50-milliliter syringe was used to inject casting material into the clamped mold.

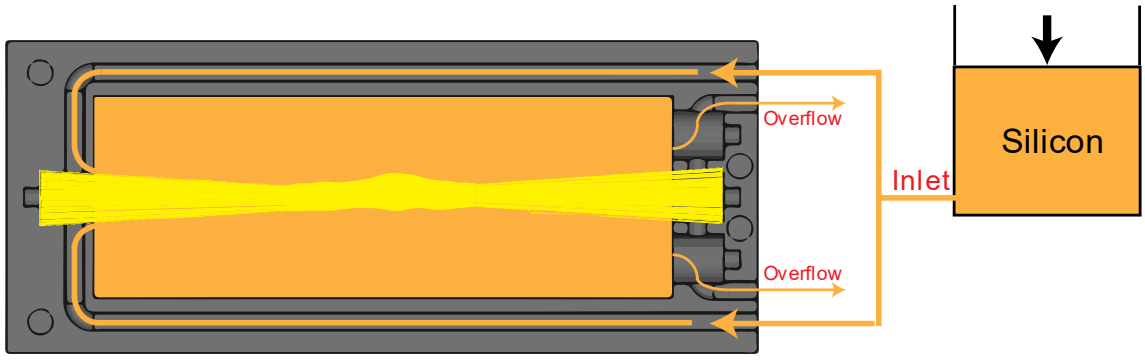

Figure 12: Silicon mold casting.
The casting of silicon mold represents the negative relief of the exterior vessel geometry of cadaveric carotid C30. The orange region represents the area to be filled with silicone rubber.

Using Oomoo 30 Tin-Cure Silicon Rubber with a ratio of one part silicon to one part curing agent by volume, a curing time of three hours ensures maximum stabilization of the material. After opening the mold and extracting the external vessel geometry, a negative relief is revealed. Cutting the silicon down to the inner vessel geometry along the meeting between the two-part mold will split the negative relief in half, with each part replicating either the top or bottom of the impeded geometry, as seen in Figure 13. This outer mold geometry will form the exterior boundary of the thin-walled phantom.

Figure 13: Exterior vessel silicon casting.
Top and bottom halves of mold with silicon relief of exterior vessel geometry of cadaveric carotid C30.

2.2.4 Thin-Wall Vessel Casting

The material used to cast the thin-walled vessel is liquid Poly-vinyl alcohol (PVA). This tissue-mimicking material is chosen for its ability to modulate its material elasticity by subjecting the PVA to varying freeze-thaw cycles [36]. Further, various concentrations of graphite powder are added to the PVA solution to alter the material's acoustic scattering characteristics.

The PVA tissue-mimicking material is prepared using the formulation outlined in Table 1 and described in [34]. The manufacturing procedure begins with the heating of distilled water on a hotplate set to 150^0C and a stir bar spinning at $120\,rpm$ to ensure even heating. Once the water reaches 45^0C the PVA powder is slowly added to prevent clumping. This procedure is continued until all PVA powder has been dissolved. The graphite powder and potassium sorbate are added similarly, and the solution is heated at 90^0C. As the solution temperature rises, the stir bar rpm must increase to

maintain proper mixing as the solution viscosity increases. However, at no point should the rpm reach a point where the central vortex pulls air into the solution. This will result in perfusion of air within the solution and will negatively affect the acoustical qualities of the tissue-mimicking material. Upon reaching 90^0C the hotplate is turned off, and with the stir bar still rotating, the solution is allowed to cool to room temperature in preparation for casting the thin-walled phantom.

Material	Density (g/mL)	Mass (g)	Volume (mL)
Distilled Water	1	179.28	179.28
PVA Powder	1.19	20.68	17.38
Graphite Powder	2.15	6.20	12.89
Potassium Sorbate	1.36	0.62	0.56
Totals		**206.78 g**	**200.00 mL**

Table 1: Poly-vinyl alcohol formulation.

To cast a thin-walled phantom, the 3D printed internal vessel geometry is placed within the same two-part mold similar to the casting of the exterior geometry; however, now the silicon relief remains. Great care must be taken when placing the internal geometry in the mold. The direction and rotation with respect to the exterior silicon relief are paramount and will determine the degree of anthropomorphism. Therefore, reference to computer geometric models should be utilized to ensure proper positioning before the casting process advances. The same methodology for applying and prestressing the two-part mold sealant should be utilized for casting preparation.

After proper alignment, the same injection process shown in Figure 11 is used to inject liquid Poly-vinyl alcohol (PVA), as seen in Figure 14. As shown in Figure 11, the upright position must be maintained when the mold is placed in a freezer to prevent unwanted PVA drainage. Each freeze cycle lasts twenty-four hours at -17^0C while the thaw cycles occur at room temperature for an additional twenty-four hours. This procedure is repeated four to six times or until the thin-walled lumen has reached the desired elasticity.

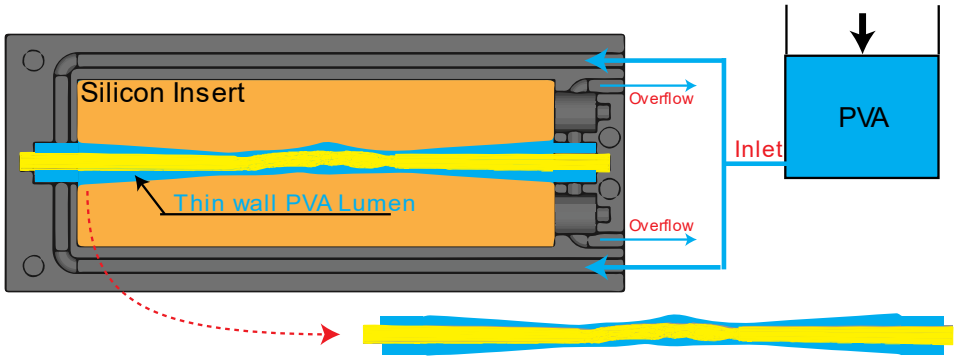

Figure 14: Thin-walled lumen casting.
The casting of the thin-walled lumen is accomplished by utilizing silicon relief of the exterior vessel geometry of cadaveric carotid C30 and its representative 3D-printed interior vessel geometry. The blue region represents the area filled with PVA and will form the thin-walled lumen.

2.3 Phantom Manufacturing Process

The manufacturing process for a thin-walled or wall-less anthropomorphic flow phantom follows the same foundational steps of acquiring an excised carotid artery, imaging with μCT, converting images to volumetric models, and 3D printing the required molds and geometries. However, depending on the phantom type, the process diverges in the final construction steps, as illustrated in Figure 19.

2.3.1 Thin-Wall Anthropomorphic Flow Phantom

The 3D-printed internal geometry supports the thin-walled phantom upon removal from the two-part mold. Removing the vessel from this support is a delicate and critical step in producing a flow phantom without introducing any ruptures in the wall. To prevent damage to the thin-walled vessel upon removal from the interior 3D model, a method of slowly pushing the vessel along and pulling the model out will allow the phantom to gradually be removed from its support. If the vessel is successfully removed without generating defects that hinder its ability to retain fluid, it can be suspended within the flow phantom box seen in Figure 15 and Figure 16. This box is laser cut using six-millimeter acrylic sheets and constructed with acrylic solvent cement. The hose couplers are 3/8" to 3/8" and held in place by a two-part adhesive consisting of epoxy resin putty and hardener putty.

After kneading and application, the adhesive putty produces a waterproof bond between the hose coupler and the acrylic box. Acoustic dampening rubber lines the parameter and bottom of the flow phantom box to reduce acoustic reverberations [37].

The tissue-mimicking material surrounding the thin-walled vessel is a gelatin graphite formulation. This material's elasticity can be modulated by altering the ratio of gelatin and the scatter properties by the ratio of graphite [38]. The formulation in Table 2 is designed to produce a material with Young's modulus of approximately $60\ kPa$ and an acoustic attenuation of approximately $0.5\ dB/cm/MHz$. This mimics the elastic and acoustic properties of the tissue surrounding the carotid artery *in vivo* [39], [40]. The manufacturing procedure begins with the heating of distilled water on a hotplate set to 100^0C and a stir bar rotating at $120\ rpm$ to ensure even heating. Once the water reaches 30^0C the gelatin powder is slowly added to prevent clumping. This is continued until all gelatin powder has been dissolved. The graphite powder and N-propanol are added in a similar manner and the solution is heated at 60^0C. Upon reaching 60^0C the hotplate is turned off and with the stir bar still rotating the solution is allowed to cool to 30^0C.

Material	Density (g/mL)	Mass (g)	Volume (mL)
Distilled Water	1	667.6	667.6
Gelatin Powder	1	86.55	86.55
Graphite Powder	2.15	55.78	25.95
N-propanol	0.8034	16	19.92
Totals		**225.93 g**	**800.00 mL**

Table 2: Gelatin graphite formulation.

The vessel mimic is positioned at twenty centimeters to replicate common *in vivo* imaging scenarios, as shown in Figure 15 [41], [42]. With the thin-wall vessel suspended within the phantom box, the gelatin graphite material can be poured slowly until the solution reaches the top of the box. Placing plastic wrap on the surface of the completed phantom can prevent defects during the cooling process. However, one additional step must be completed before imaging to ensure good ultrasound

image quality. Once cooled, the top millimeter of the phantom must be washed off with hot water to remove excess graphite that may have collected at the surface during the cooling process. This step results in the complete fabrication of a thin-walled anthropomorphic flow phantom, as illustrated in Figure 16 and Figure 17.

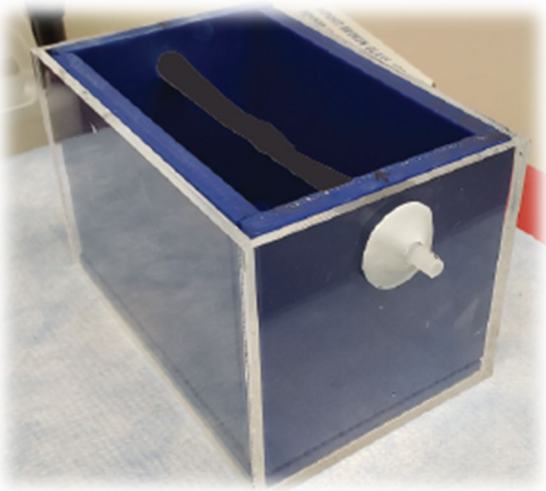

Figure 15: Suspension thin-walled vessel C30.

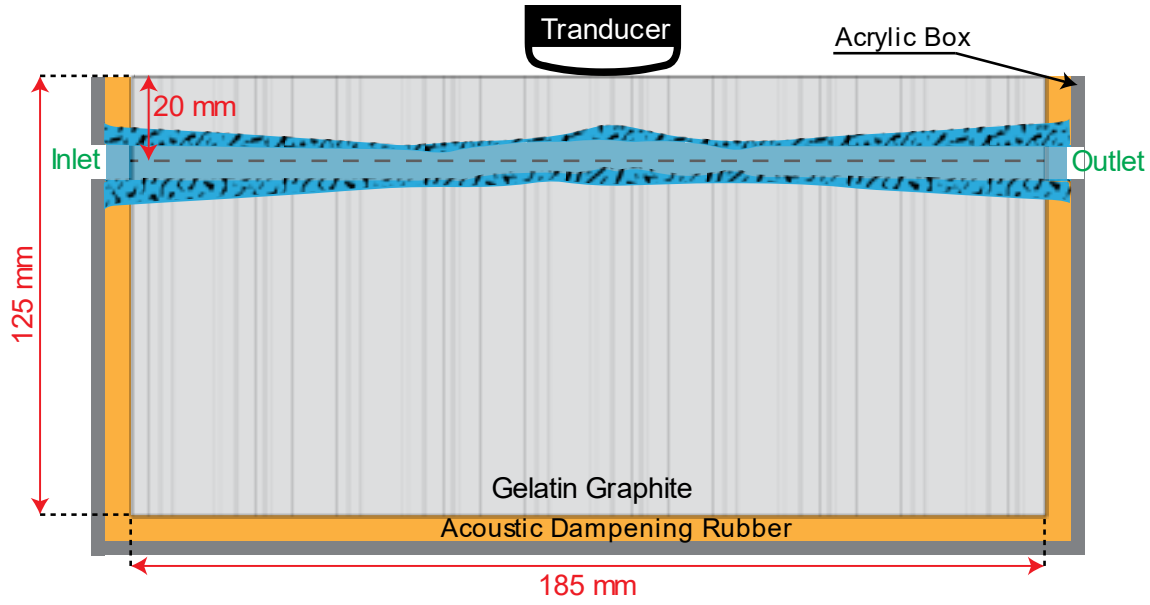

Figure 16: Embedding thin-walled lumen into flow phantom.

The thin-walled PVA phantom is suspended between the inlet and outlet of the acrylic box lined with acoustic-dampening rubber to decrease acoustic reverberations. The acrylic box has a height of 125 mm, is 185 mm long, and has a depth into the page of 125 mm. The lumen is filled with water to prevent the vessel from collapsing when gelatin graphite tissue mimicking material is poured into the acrylic box to surround the thin-walled phantom.

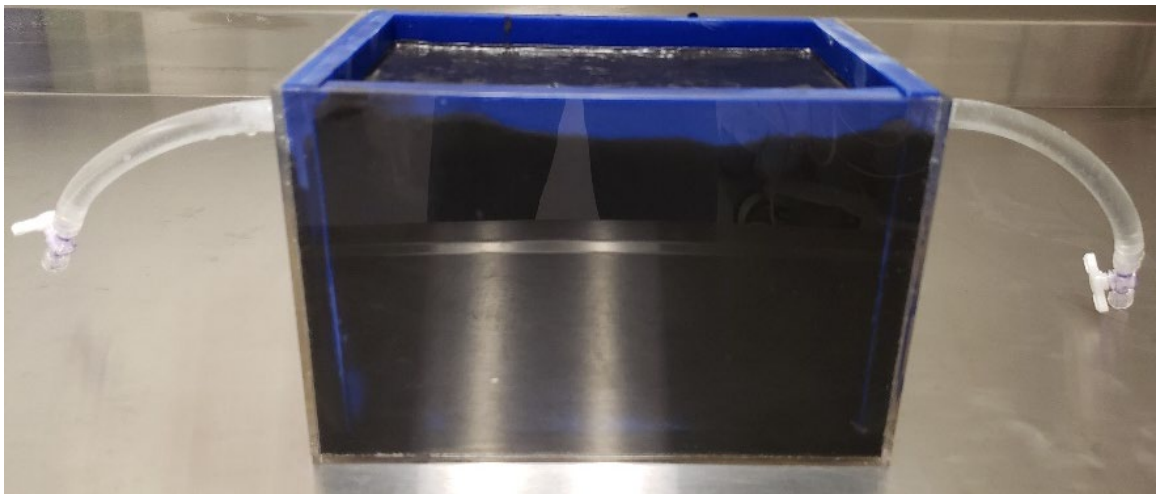

Figure 17 Fabricated anthropomorphic thin-walled lumen flow phantom.

2.3.2 Wall-less Anthropomorphic Flow Phantom

Production of a wall-less anthropomorphic flow phantom begins similarly to the thin-walled phantom with the 3D printing of the internal vessel geometry. This positive relief of the internal geometry is suspended between the inlet and outlets of a flow phantom box identical in dimensions and construction to that of the thin-walled flow phantom minus the hose couplers. A tissue-mimicking material identical to the gelatin graphite formulation given in Table 2 is poured into the flow phantom box, and the internal geometry is removed after solidification, as in Figure 18. The internal geometry must be removed with the utmost care and delicacy so as not to damage the inner contours of the vessel wall. Changes in lumen diameter and vessel profile result in material strain of the gelatin graphite tissue mimicking material as the 3D-printed inner geometry is withdrawn from the phantom. Water is injected and sealed inside with plumbing fixtures to stabilize the lumen shape and support the vessel wall, as illustrated in Figure 18 Panel B). This procedure produces a simple wall-less anthropomorphic flow phantom.

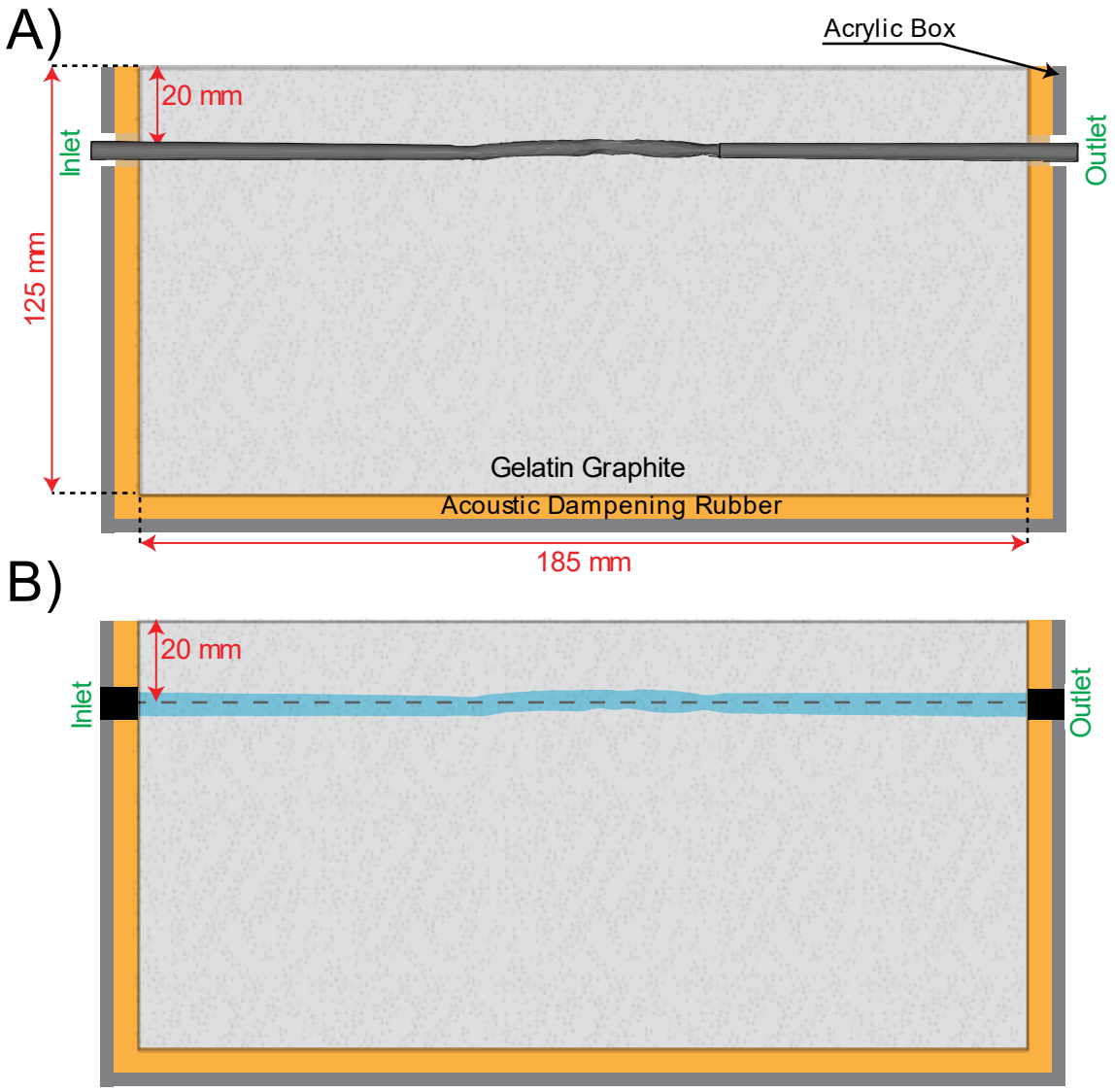

Figure 18: Wall-less phantom casting.

A) Interior vessel geometry of cadaveric carotid C30 is suspended at a depth of twenty millimeters from the surface of the flow phantom acrylic box. Gelatin graphite tissue mimicking material is poured into the acoustically dampened box. ***B)*** *Interior vessel geometry of cadaveric carotid C30 is carefully removed to leave the relief of the desired vessel geometry. Water is placed into the vessel, and ends are capped to prevent damage to geometry.*

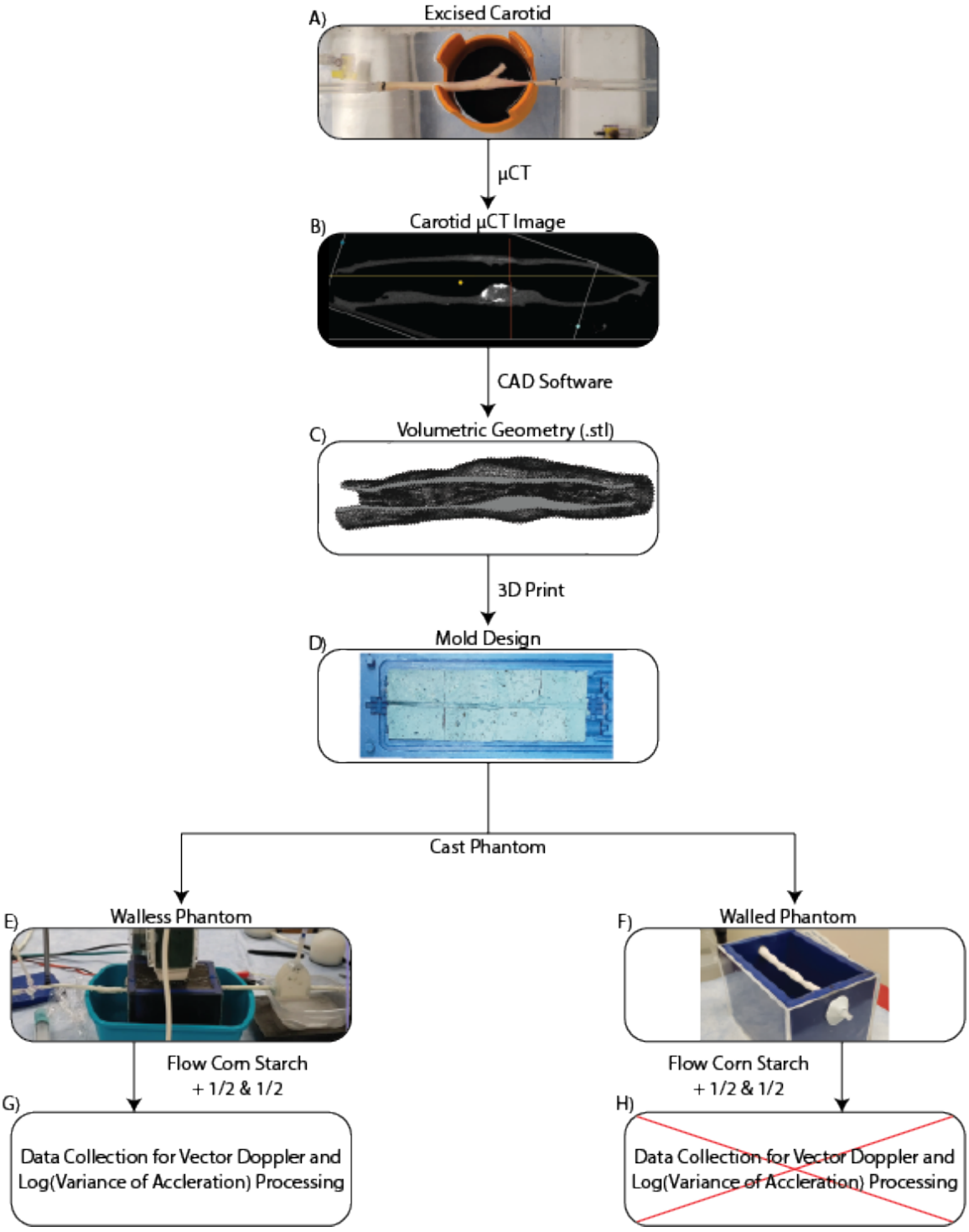

Figure 19: Anthropomorphic flow phantom modeling, construction, and testing.
A) Excised human carotids sourced from the University of North Carolina Autopsy Services fixed in 10% formalin solution. ***B)*** *Fixed carotid is imaged using a micro–Computed Tomography to obtain interior and exterior vessel geometries.* ***C)*** *Vessel geometry is smoothed and processed to prepare internal and external geometries to be printed using additive manufacturing techniques.* ***D)*** *Molds using vessel geometries are developed to construct thin-walled and wall-less phantoms.* ***E & G)*** *Wall-less phantom is cast using C30 internal vessel geometry, and gelatin graphite tissue mimicking material and is imaged using a mixture of corn starch and half and half as blood mimicking fluid to simulate blood flow.* ***F & H)*** *Thin-walled phantom is cast using PVA thin-walled vessel and gelatin graphite tissue mimicking material surrounding. Phantom is imaged using a mixture of corn starch and half and half as blood-mimicking fluid to simulate blood flow; however, due to vessel rupture, data processing was unsuccessful.*

2.4 Experimental Setup

The anthropomorphic flow phantom described in the section above is connected to the experimental setup developed by Anand *et al.* [43], as illustrated in Figure 20. Blood-mimicking fluid is pumped through the phantom by a peristaltic pump at a constant flow rate of 300 mL/min. This fluid is composed of a mixture of one liter of half & half (grade A, homogenized, ultra-pasteurized, dairy product) to fifty grams of one hundred percent pure corn starch and was developed by Anand *et al.* [43]–[45] to replicate the viscous properties of human blood. A reservoir with a magnetic stir bar is needed to prevent the corn starch from settling out from the half & half. The peristaltic pump is directly downstream from the reservoir to minimize the resistance the pump must pull. Directly after the pump, a pulse dampener is positioned. This device smooths out the rapid pulsations of the pump by maintaining a cushion of air at the top of the dampener. As the peristaltic pump maximizes the pressure of the system, the air pocket slightly compresses and absorbs energy; hence, the system's flow rate will be smoothed and will not exhibit the rapid pulsations of the pump rotor. This mechanism will allow for steady-state flow conditions to be assumed while processing the ultrasound flow data. Downstream of the pulse dampener and before the flow phantom, thirty-five centimeters of pipe are required to ensure fully developed flow upon entering the imaging region. This length was selected to provide ample distance for the blood-mimicking fluid to form a fully parabolic flow profile and to minimize any boundary layer effects.

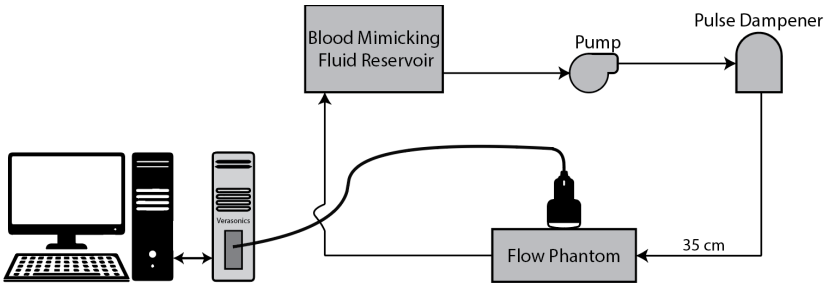

Figure 20: Experimental flow setup.

2.5 Data Acquisition

To measure the vessel geometry, flow profile, and wall shear stress of the anthropomorphic flow phantom, a Verasonics Vantage 256 ultrasound system was programmed by Keerthi Anand to collect both vector Doppler and acoustic radiation force impulse (ARFI) data using compounded plane waves [28]. Vector Doppler data is needed to estimate the wall shear stress along the vessel wall, while acoustic radiation force data is used to delineate the lumen boundary from the background tissue. The sequence (illustrated in Figure 21) begins with a reference tracking pulse composed of three plane wave pulses of $-5^0, 0^0, +5^0$ angles. The three angles will be coherently compounded to form a reference image under zero displacement. A single radiation force push, 500 cycles long, centered at 4.21 MHz, and focused on the bottom wall of the phantom lumen causes an ARFI-induced displacement and an associated shear wave to propagate outwards. This tissue disturbance is recorded by a series of one hundred tracking pulses, each composed of the same three angles as the reference track, as was done by Anand *et al.* [28].

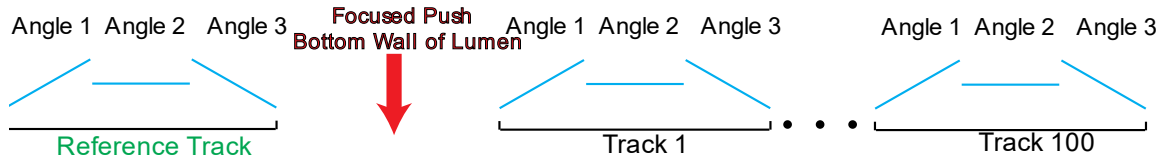

Figure 21: Vantage ultrasound sequence
A reference track composed of three plane wave pulses at different inclinations is used as the baseline of tissue with zero displacements. A radiation force push follows this pulse sequence focused on the bottom wall of the lumen and centered within the field of view. Tissue displacement is tracked through one hundred subsequent tracking pulses with the same composition as the initial reference track.

2.6 Data Processing

2.6.1 Normalized Log(VoA) Estimation

Using the methods Anand et al. [39] developed, the raw radiofrequency (RF) data gathered from the Verasonics Vantage ultrasound system was beamformed using plane-wave coherent compounding. Each of the three angled plane-wave transmits within each tracking sequence was beamformed along five separate angles $(-10^0, -5^0, 0^0, +5^0, +10^0)$. These five beamformed receive

images are coherently compounded to represent a single angle transmitted within one tracking sequence time point. This processing step is represented in Figure 22 as the beamforming of multiple angles and the first level of coherent compounding. This data is saved in the computer's memory for the vector Doppler processing; however, to calculate the Log (Variance of Acceleration) of the image, the data must be further processed to perform displacement estimation.

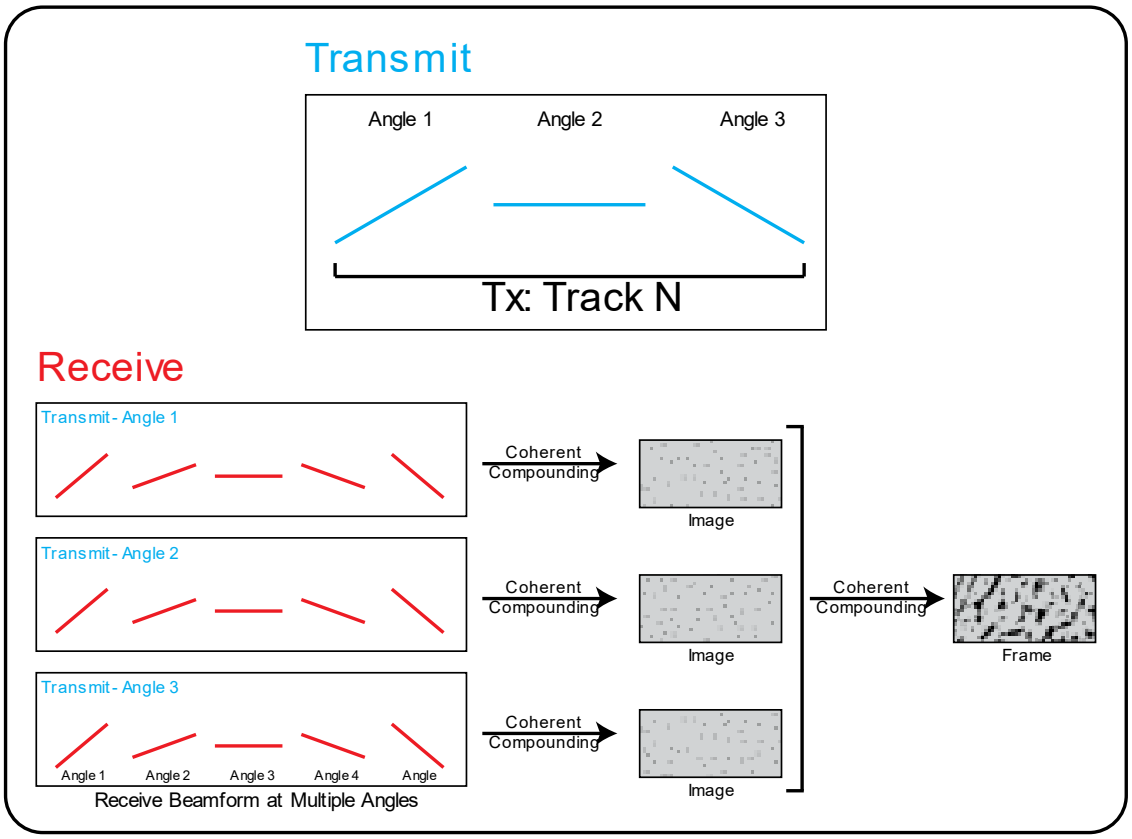

Figure 22: Receive beamforming.
Each track pulse is composed of three plane wave transmits at varying degrees of inclination. Upon beamforming, each transmit pulse is beamformed at five different angles and compounded to form an image. After all three transmit angles are processed, compounding occurs, forming an image that represents a single frame of the tissue displacement in time after the AFRI push.

Each of the three beamformed transmit angles resulted in a reconstructed image consisting of five receive angles. These three reconstructions are coherently compounded to form a frame representing tracking pulse N in Figure 22. As additional tracking transmit angles are processed, a walking kernel is established to form subsequent frames. Figure 23 demonstrates a walking kernel and how it increases the number of generated frames. Once all one hundred tracking pulses are processed

into an ensemble of images representing the tissue recovery after the ARFI push, tissue displacement estimation is performed.

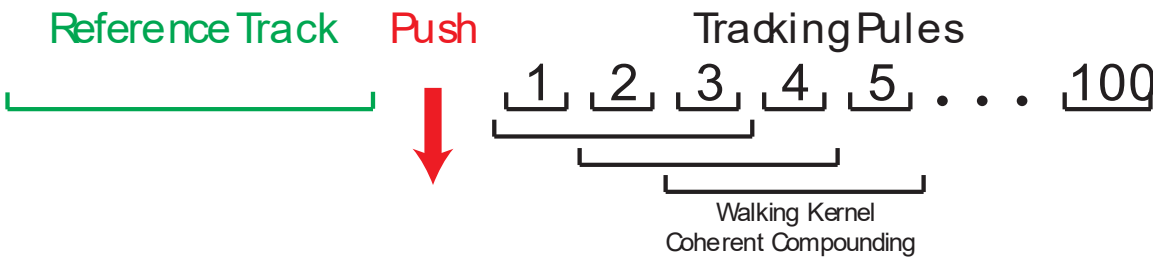

Figure 23: Walking kernel coherent compounding

Using the reference track as a zero-displacement baseline, two-dimensional normalized cross-correlation is calculated for each tracking pulse, and the peak displacement image is found for each frame. Using the ensemble of displacement through time, the variance of acceleration (VoA) is calculated by finding the variance of the second time derivative of the tissue position time series. This parameter offers insights into the carotid plaque characteristics by delineating LRNC, IH, CD, collagen, and fibrous cap thickness [29], [46], [47]. Log(VoA) can also distinguish between the background tissue and blood flow through the rate of temporal tissue decorrelation. Within one ensemble, the fluid flow will exhibit larger displacements than the vessel wall and will, therefore, decorrelate more quickly [43]. By taking the Log transformation, the Log(VoA) image is constructed and is normalized $[0\ 1]$ to median $\pm$ 3 MAD (Mean Absolute Deviation) using a region above and below the lumen. This technique enhances the Log(VoA) image contrast between the phantom lumen and the background gelatin graphite tissue mimicking material.

2.6.2 Vector Doppler Estimation

After the normalized Log (VoA) is calculated in the data processing pipeline, a vector Doppler algorithm is applied to the five beamformed receive angles over a kernel of thirty tracking pulses. The Lupus phase-based motion estimation algorithm estimates the phase shifted along each beamformed angle over a temporal kernel of thirty tracking pulses. This algorithm gives the estimated fluid flow

velocity away from or towards the direction of the beamformed angle. Since multiple angles are reconstructed, a least square vector Doppler algorithm is used to find the flow magnitude and direction throughout the image. However, since the beamformed angles do not all overlay, as illustrated in Figure 24, due to the inclination of the steered angles, there are regions over which the least squares vector Doppler algorithm does not produce reliable estimations. For this reason, the flow map in Figure 25 panel C) is cropped to isolate the region over which the flow estimations are trustworthy.

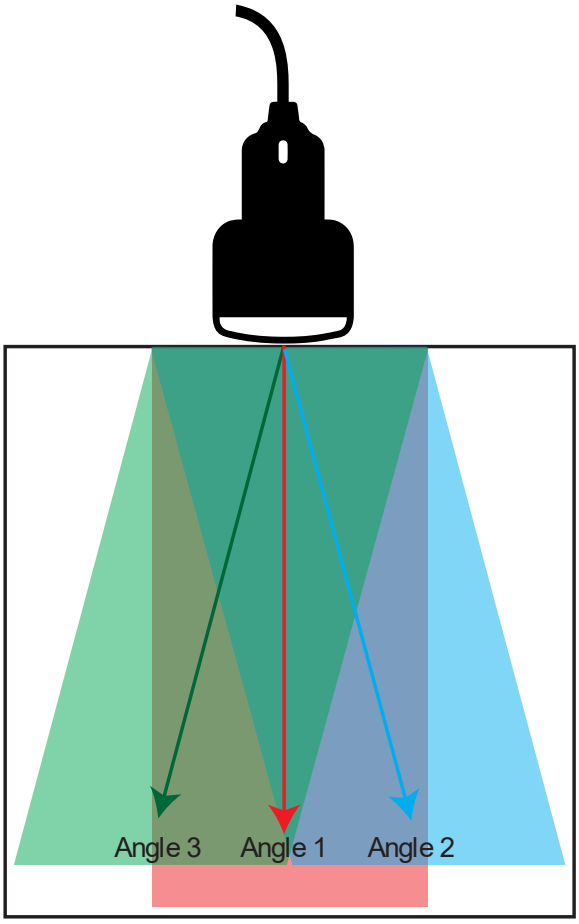

Figure 24: Least squares vector Doppler

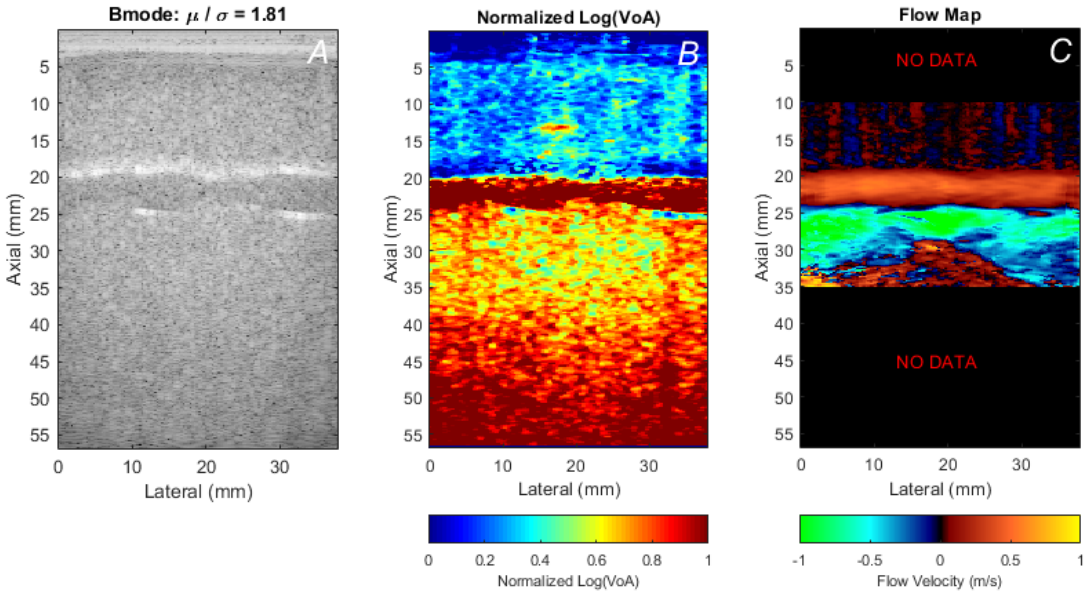

Figure 25: B-mode, Normalized Log(VoA), and Flow Map

A) Flow phantom B-mode image with μ/σ =1.81. B) Normalized Log(Variance of Acceleration) image of flow phantom. C) Fluid velocity image reconstructed from vector Doppler algorithm.

2.6.3 Vessel Wall Segmentation

To calculate the wall shear stress (WSS) upon the vessel, the wall boundary must first be segmented. Using the methodology developed by Anand *et al.* [28], an initial segmentation attempt of the fluid flow from the surrounding phantom material is accomplished by thresholding the normalized Log (VoA) image, see Figure 26 Panel A). A threshold of 0.9 on the normalized scale was chosen to maximize the area identified correctly as the lumen and minimize the area identified as false positives. This rudimentary segmentation does not provide a clean representation of the flow profile, as seen in Figure 26 Panel A), due to many holes within the lumen and false readings outside the known flow profile. To reduce these artifacts, a filling operation is used that will solidify the known flow area in Panel B). Then closing and opening operations are performed to reduce the number of false readings outside the lumen, Panel C). This procedure results in a mask that is used to identify the image coordinates of the lumen, Panel D). By overlaying the segmented wall coordinates upon the normalized Log(VoA) image used in the vessel segmentation process in Figure 27, it can be confirmed that the procedures developed by Anand *et al.* can effectively delineate the vessel wall [28].

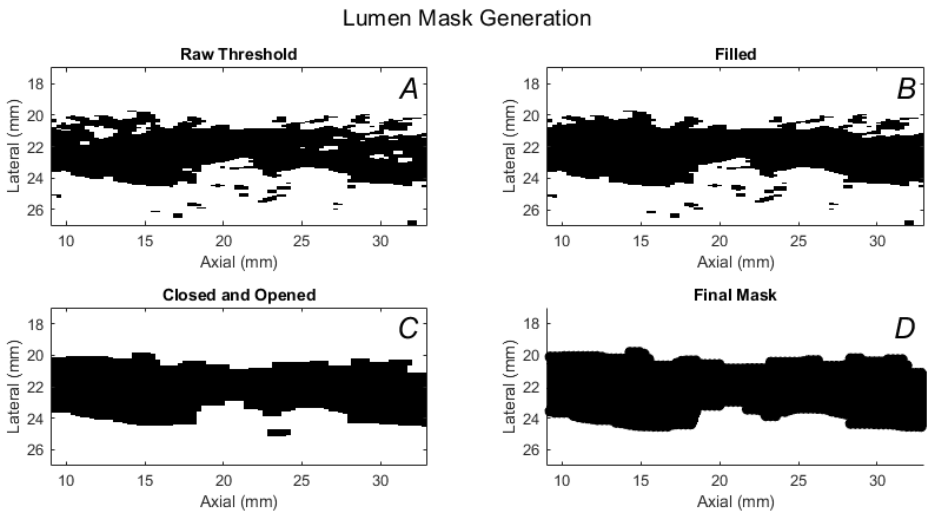

Figure 26: Lumen Mask Generation

A) Lumen segmentation using normalized Log(Variance of Acceleration) with a threshold of 0.9. B) Filling operation applied to the raw threshold to removed holes inside the flow area. C) Closing and opening operations are applied to the filled mask to remove noise from segmentation. ***D)*** *Median filter applied to closed and opened mask to smooth rough edges and identify lumen wall coordinates.*

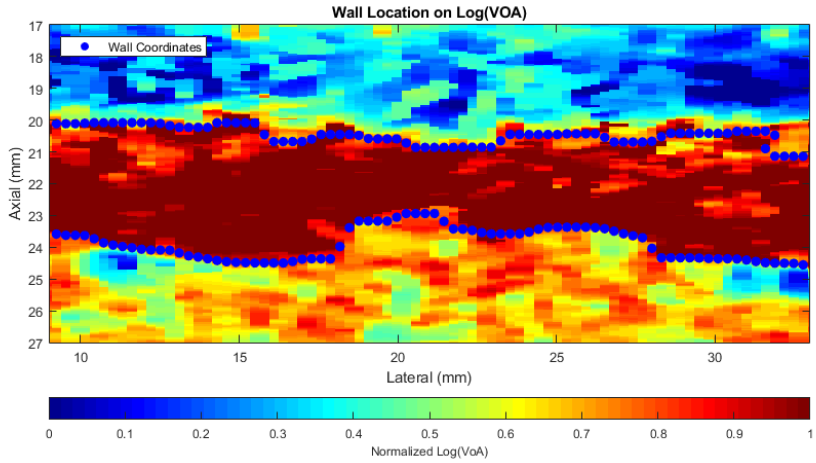

Figure 27 Lumen wall coordinates overlayed on normalized Log (Variance of Acceleration).

2.6.4 Wall Shear Stress Calculation

Calculating the wall shear stress (WSS) upon the vessel wall boundary was accomplished using the approaches developed by Anand *et al.* [28]. These techniques require the velocity profile across each lumen axial slice to fit with a parabola velocity distribution. This parabolic flow profile is an assumption derived from the data acquisition experimental inlet condition. Because ample tubing before the vessel was given, the flow profile within the lumen can be expected to be fully developed and laminar, thus, providing a parabolic profile [8]. Figure 28 demonstrates the experimentally calculated velocity profile with the vessel segmentation overlay. Each slice between the top and

bottom wall produces a velocity profile with the known wall position velocities set to zero to satisfy the established no-slip condition [23], [28]. The spatial velocity gradient at the vessel wall multiplied by the fluid viscosity of the blood-mimicking fluid gives an estimate of the wall shear stress. Repeating this procedure at all wall locations produces a wall shear stress estimation along the top and bottom wall of the flow phantom as demonstrated by Figure 28.

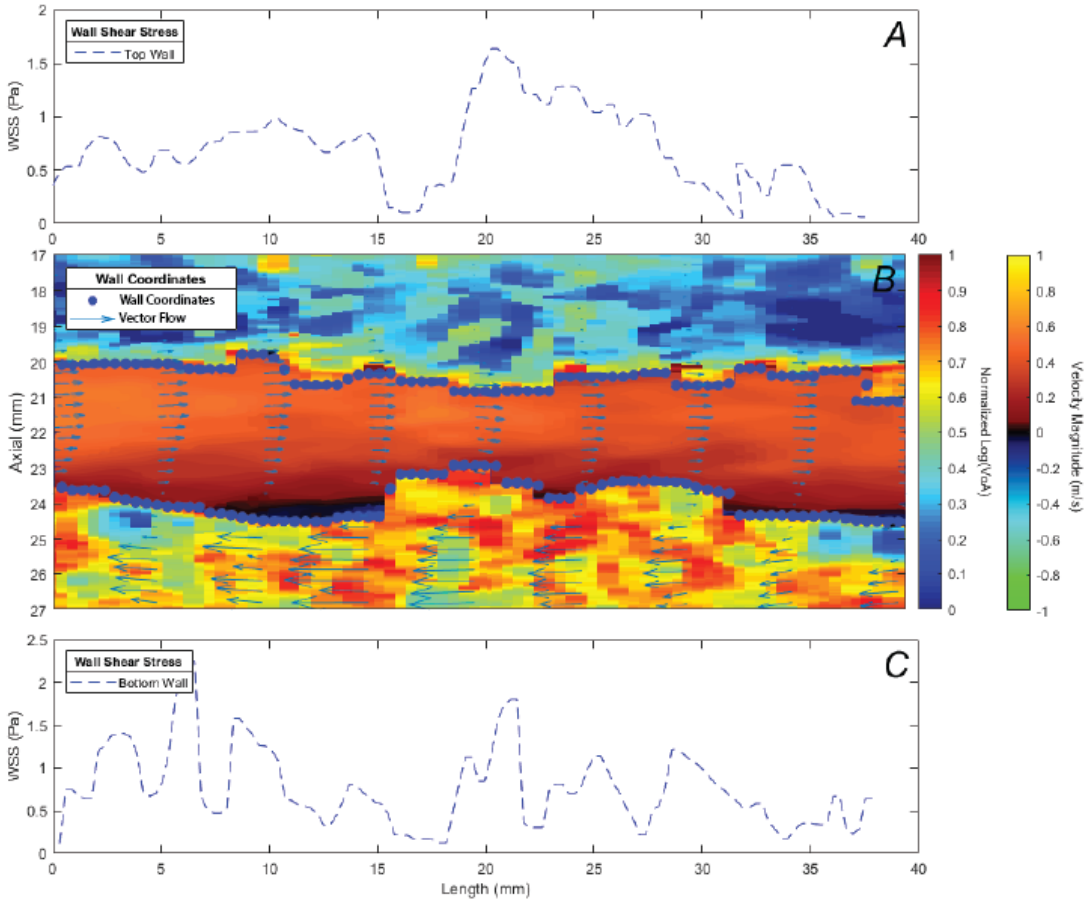

Figure 28: Flow Phantom Wall Shear Stress

A) Top wall shear stress profile of phantom data. B) Experimentally detected wall coordinates overlayed on velocity magnitude map inside lumen area and Normalized Log (Variance of Acceleration) outside with vector doppler arrows indicating the direction of detected fluid flow. ***C)*** *Bottom wall shear stress profile of experimental phantom data.*

2.6.5 Fluid-Structure Interaction Correlation

To judge the extent to which the phantom recapitulates the flow in the modeled human plaque, a comparison must be made to a standard that encompasses the vessel geometry and calculates the wall shear stress. For this purpose, a fluid-structure interaction (FSI) model is utilized that was developed by Anand with the collaboration of Kolahdouz *et al.* [48]. The smoothed vessel geometry segmented from the micro-CT and fluid flow characteristics are employed by the FSI model to estimate the wall shear stress throughout the vessel geometry. Figure 29 displays the full volumetric wall shear stress model with the selected sliced used to correlate with the experimental flow phantom data.

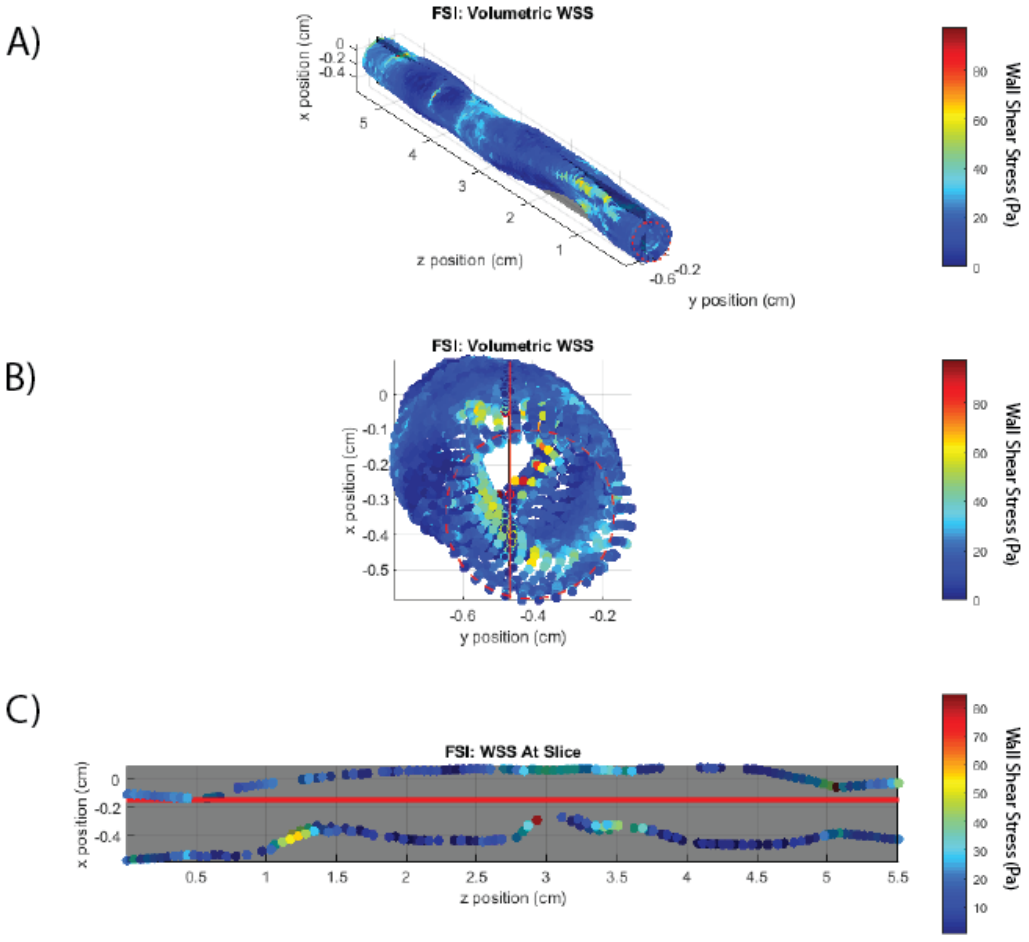

Figure 29: FSI Correlation

A) Fluid-structure interaction model volumetric wall shear stress of cadaveric carotid C30 along the entire vessel. B) Axial view of volumetric wall shear stress with outlet geometry identified with a red dotted circle and a vertical red line indicating slice represented in panel C. C) Fluid-structure interaction model wall shear stress of cadaveric carotid C30 at the slice of interest. The red centerline divides the top wall coordinates from the bottom wall.

CHAPTER 3: RESULTS

3.1 Completed Flow Phantoms

3.1.1 Thin-Wall Anthropomorphic Flow Phantom

The construction of a thin-walled anthropomorphic flow phantom proceeded successfully up to the step represented by panel H) of Figure 19. The failure of the flow phantom to produce useable data originated from two malfunctions. The first is the stretching of the PVA thin-walled vessel upon suspension in the flow phantom box. The vessel's weight and the material's nature resulted in plastic strain deformation from the applied force of gravity. The central span of the vessel was not located at the intended height and instead sagged before pouring the gelatin graphite tissue-mimicking material. Upon submersion, the elongated vessel was filled with water to retain the cylindrical vessel geometry. This difference in density between the thin-walled vessel and the higher-density tissue-mimicking material resulted in a buoyant force. This force pushed the vessel to the surface of the lumen as illustrated in Figure 30. The incorrect location fractured the anthropomorphism of the flow phantom. Furthermore, the failure of the vessel to retain fluid due to a hole in the wall resulted in an inoperable thin-walled anthropomorphic flow phantom.

Figure 30: Thin-walled lumen malfunction.
Vessel surfacing after embedding walled phantom into gelatin graphite matrix. Lower density surrounding generated buoyant force resulting in vessel ascension to break the surface of the anthropomorphic carotid flow phantom

3.1.2 Wall-less Anthropomorphic Flow Phantom

In contrast to the limitations of the thin-walled phantom, the wall-less anthropomorphic flow phantom exhibited durability under constant unpressurized flow. The phantom constructed using C30 cadaveric carotid geometry retained flow up to 300 mL/min. Additionally, the scattering properties of the tissue-mimicking material resulted in a $\mu/\sigma = 1.81$, see Figure 25. This value nearly equals the fully developed scatter value of $\mu/\sigma = 1.9$ [49]. When additional flow conditions were applied with a pressurized pseudo cardiac flow, the strain on the vessel wall exceeded the fracture strain and resulted in rupture. This impaired further investigation of the flow phantom; however, not before the required sequences were acquired to quantify the agreement between the experimental flow phantom and the FSI model.

3.2 Experimental and FSI Correlation

The top wall shear stress comparison between the C30 flow phantom and its representative FSI counterpart of Figure 31 indicates similar WSS trends; however, they do not correspond in exact values. This tendency extends to the bottom wall, yet there is one significant deviation between experimental data and the FSI model at around twenty-seven centimeters. At this point, the FSI model peaks, and the phantom data takes a local minimum. Near the vessel stenosis around twenty-one centimeters, the FSI model and phantom data show close coupling of the plaque geometry and the adherence between the two procedures phases in and out throughout the vessel length. These incongruities, however, do not alter the characterization of the plaque rupture risk. Since the absolute threshold for high and low WSS depends on concomitant conditions and systemic factors, the deviations between the experimental phantom and FSI model would not alter the vessel's classification as atheroprone, atheroprotective, or rupture-prone [10].

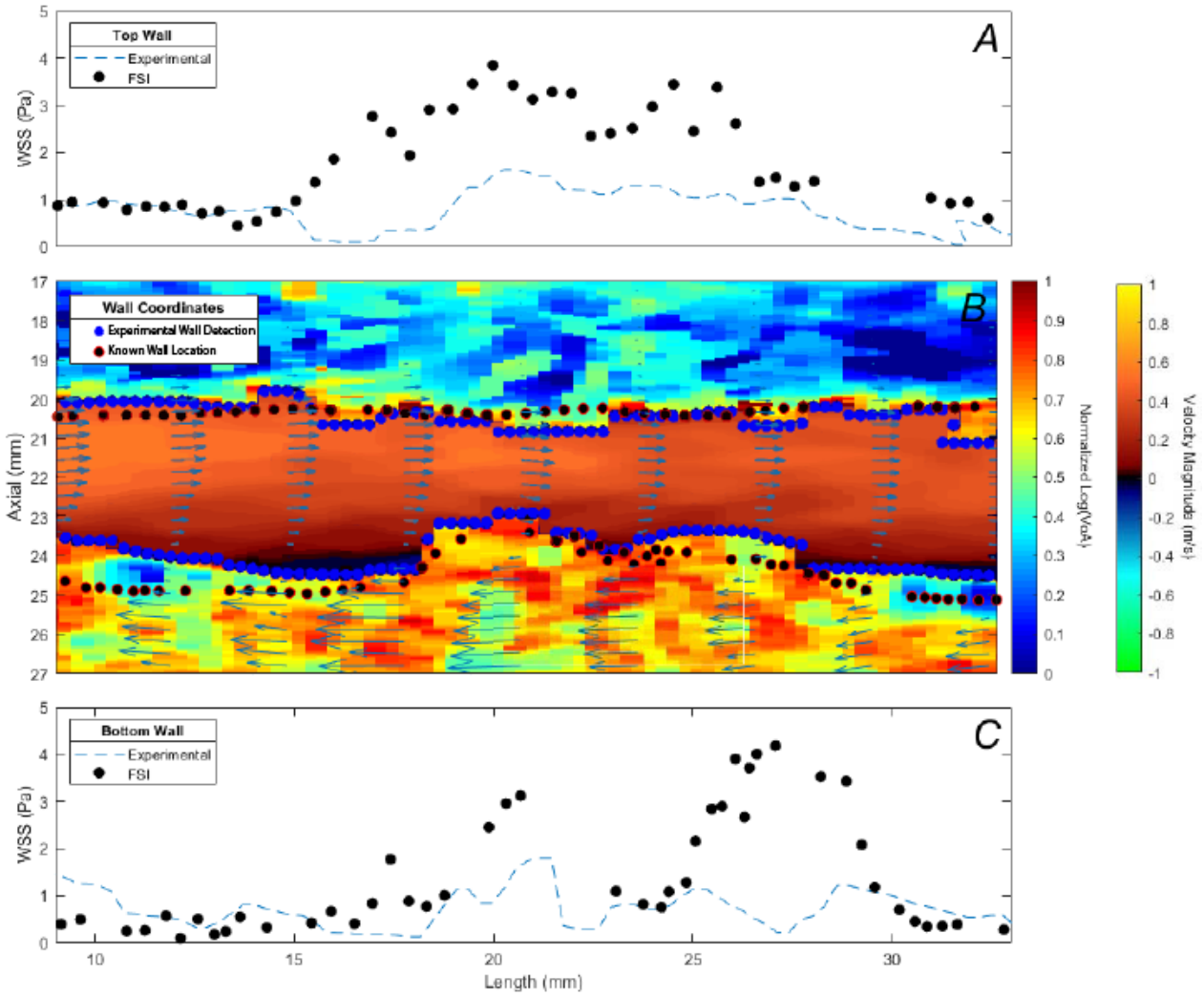

Figure 31: C30 Anthropomorphic flow phantom and FSI model comparison

A) Top wall shear stress profile comparison of experimentally detected and fluid-structure (FSI) model simulations. B) Experimentally detected and FSI wall coordinates overlayed on velocity magnitude map inside lumen area and Normalized Log (Variance of Acceleration) outside with vector doppler arrows indicating the direction of detected flow. C) Bottom wall shear stress profile comparison of experimentally detected and fluid-structure (FSI) model simulations.

CHAPTER 4: DISCUSSION

4.1 Phantom Merits

4.1.1 FSI and Phantom Correlation

Modulating anthropomorphic flow phantom geometries for subsequent use for ultrasound beam sequence and signal processing advancement is permissible due to the experimental flow data WSS and wall identification matching with the FSI validation counterpart. This correlation between experimental estimation and model calculation illustrated in Figure 31 demonstrates a degree of validation that the flow phantom recapitulates the expected WSS. This confirmation allows for the modulation of vessel geometry that will not reduce the degree to which the modified flow phantom would recapitulate its FSI equivalent. Consequently, the phantom fabrication process illustrated in Figure 19 can be replicated using modified mold and tissue-mimicking materials such that adherence to feasible physiological hemodynamic flow environments is not violated. Therefore, it can be concluded that the constructed anthropomorphic phantom supports flow conditions that create WSS as expected for the modeled complex geometry.

4.1.2 Mold Customization

The ability to modulate cadaveric carotid 3D models to alter the level of stenosis and plaque geometry is a crucial characteristic of the thin-walled and wall-less anthropomorphic flow phantoms. By imaging a single human carotid with micro-CT, multiple flow phantoms can be produced by varying the physical attributes and geometries of the vessel. Modulating the thin-walled vessel material elasticity and scattering properties through manipulating the PVA formulation and number of freeze-

thaw cycles, and graphite particle concentration allows for developing vessels with varying acoustic properties. Additionally, adjustments to the background gelatin graphite tissue mimicking material allow for the augmentation of the acoustic qualities of the finished anthropomorphic flow phantom. Vessel geometry transformation is achieved by altering either interior or exterior CAD models to produce any number of hemodynamic circumstances. Higher degrees of stenosis or less favorable entrance conditions are conventional examples of such changes.

The utility of mold customization is the independence from additional human cadaveric carotid arteries. From a single human carotid, many flow phantoms can be generated with a high degree of flexibility to test combined vector Doppler and plaque composition algorithms similar to Anand *et al.* [43]. Each cadaveric carotid has high variability in plaque composition and hemodynamic flow conditions; consequently, each carotid's composition and fluid dynamics may not be entirely suitable for the desired ultrasound imaging scenario. Additionally, the inconsistent and unpredictable donation of carotids results in variability of testing capacity. Finally, carotid tissue decay demands that experiments must be executed immediately upon reception. This concern results in expedited experimentation that may require lengthy research hours to ensure vessel integrity during testing. By utilizing anthropomorphic flow phantoms, ultrasound sequence development can be planned and targeted toward specific flow or geometric scenarios. Due to the limited one-time use of cadaveric carotids, different beam sequences cannot be tested and compared in the exact same geometry. This problem is overcome by utilizing flow phantoms as they can be used multiple times within their shelf-life of several weeks and can be remade long after to revisit prior imaging conditions.

For example, phantoms with high degrees of stenosis, high or low vessel elasticity, or varying lumen cross-section geometry can be fabricated, and the effect on vector doppler or AFRI sequence can be ascertained to advance future development.

4.2 Limitations

4.2.1 Data Acquisition and Processing

Although Figure 31 shows a correlation for the geometry and wall shear stress (WSS) between the experimentally calculated flow phantom and the FSI model, there are limitations to this comparison. Firstly, there is no true validation standard for WSS measurements beyond direct sensing, which is outside current capabilities. Additionally, the current techniques for acquiring and processing flow phantom WSS data are still under development by Anand *et al.* [43]. Figure 29 illustrates that the vector flow algorithm detects fluid flow outside the normalized Log(VoA) wall segmentation. This artifact arises from the elevational sensitivity of the ultrasound probe. Figure 32 shows the matching between the true flow diameter directly under the transducer and the detected flow diameter. Since the transducer is located directly above the center of the lumen, the greatest diameter is detected. Therefore, no flow is written into an area outside what is expected. Alternatively, when the transducer is shifted 1.25 mm in either direction, the expected flow diameter decreases significantly due to the curvature of the cylindrical tube. The expected flow diameter of the slice directly under the transducer is 3.75 mm; however, due to the fixed elevational sensitivity of the L7-4 ultrasound probe used by Anand *et al.* [43], the detected flow is beyond the anticipated flow diameter. The resulting flow diameter of 4.85 mm is a thirty percent increase from the expected. As shown in Figure 29: FSI Correlation, the FSI slice that matches the experimental flow data is not in the center of the vessel. Consequently, the experimental flow data will behave similarly to the concepts illustrated in Figure 33. Additional difficulties in obtaining reliable flow data are encountered when the coupling between the phantom entrance tube and the vessel is not perfectly parallel. It has been shown that any deviation in parabolic and parallel flow significantly impacts the calculated WSS [50].

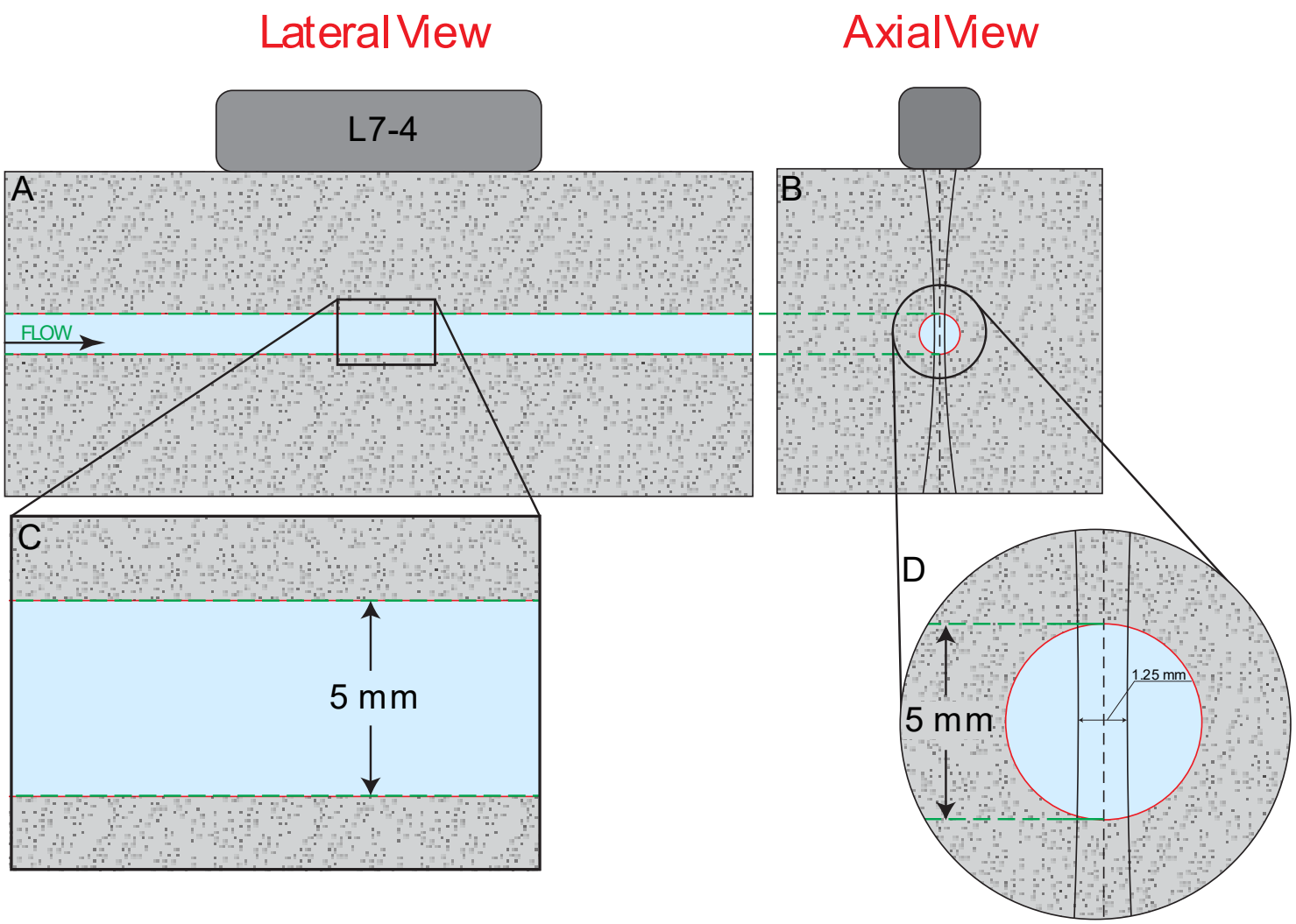

Figure 32: Ideal flow estimation.

A) Flow phantom lateral slice. B) Axial slice with the elevational region of sensitivity centered on the dotted line and bounded by solid lines. ***C)*** *Enlargement of comparison between true and detected flow areas at the center of the elevational slice.* ***D)*** *Enlargement of elevational sensitivity on the cross-section of the flow area.*

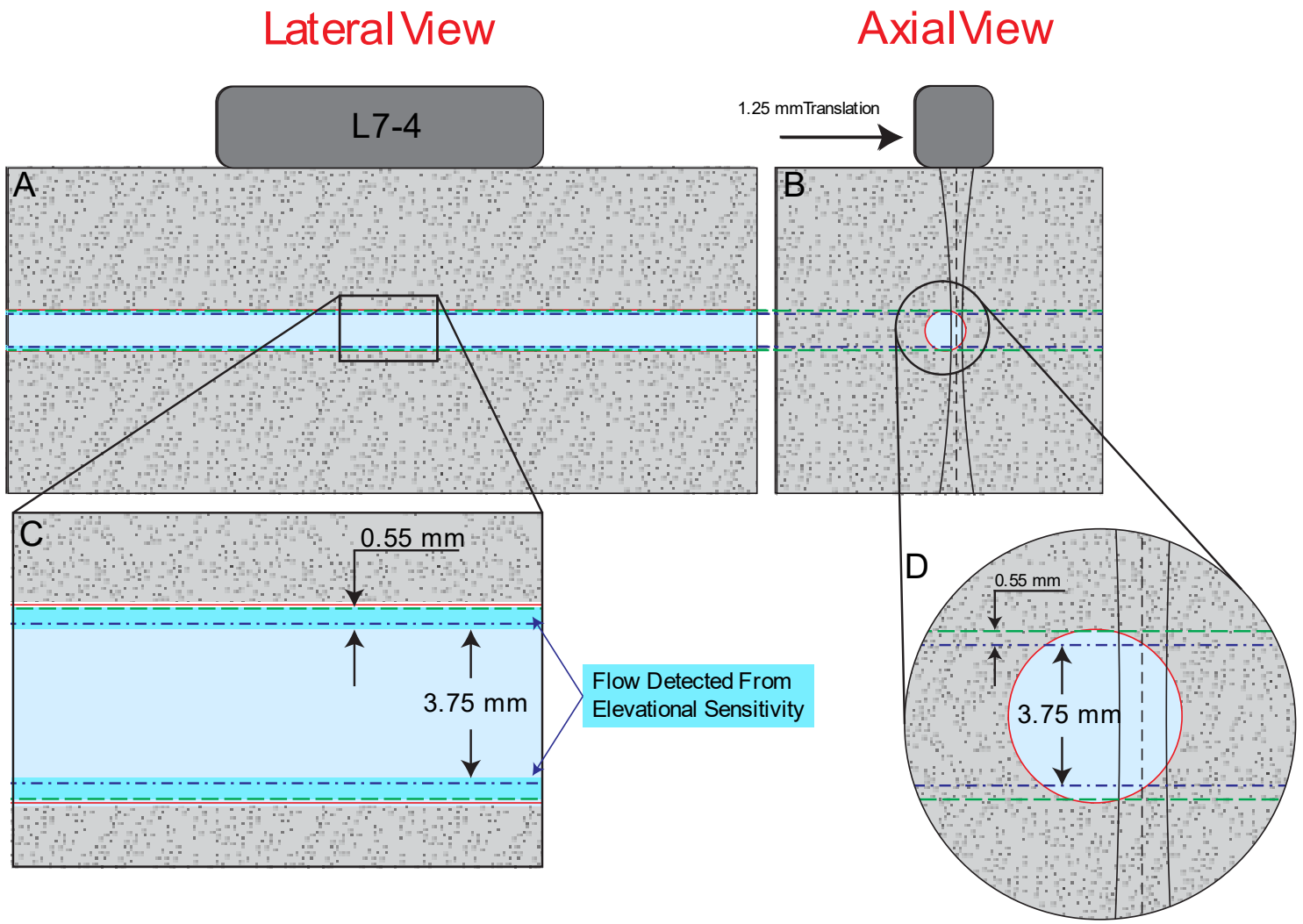

Figure 33: Flow estimation limitation.

Figure 7. A) Flow phantom lateral slice. B) Axial slice with the elevational region of sensitivity centered on the dotted line and bounded by solid lines. ***C)*** *Enlargement of comparison between true and detected flow areas at the center of the elevational slice.* ***D)*** *Enlargement of elevational sensitivity on the cross-section of the flow area under a translation of 1.25 mm to the right. `*

4.2.2 Fabrication Techniques

The manufacturing process to construct thin-walled and wall-less anthropomorphic flow phantoms is subject to high defect rates, particularly in casting thin-walled vessels. The precision required to craft vessels with wall thicknesses approaching less than a millimeter is exceptionally intensive and requires multiple attempts to produce a successful product. When positioning the inner vessel geometry for thin-walled phantom casting, as illustrated in Figure 14, any deflection in the 3D printed model or incorrect rotation can result in contact between the inner and exterior vessel geometries. Any unwanted contact will not allow PVA to infuse the entire mold and will generate hole defects in the vessel wall. Due to the nature of the PVA vessel, repair of the break is not possible. This limitation is derived from the inherited elastic characteristics of the PVA from the number of freeze-thaw cycles. Since repair requires bonding a PVA patch to the defect, the patch and the supporting bond will not possess identical elastic properties to the vessel. Therefore, defect repair is inappropriate for the original vessel, and a replacement vessel must be constructed with a matching number of freeze-thaw cycles. However, a repair patch could model a soft feature in the vessel wall and utilize the defect to find utility for the flow phantom. The difficulty in fabricating thin-walled flow phantoms may require several weeks to produce a vessel of sufficient quality and integrity to sustain flow without leaking blood-mimicking fluid.

Additionally, these thin walls are subject to breaking upon pressurization during pseudo-cardiac pulsatile flow. This limitation may derive from the inadequate elasticity of the vessels despite the proper design, phantom formulation, and fabrication. Due to the small amounts of PVA required and the thin-walled nature of vessel construction, the rate of freeze-thaw cycles deviates from that of published bulk PVA. Material properties outlined in the literature specify the elastic modulus of PVA-based tissue-mimicking materials for large-volume samples [36], [51]. However, reference to the Handbook of Heat Transfer [52] reveals the impact of surface area and volume on the heat transfer

rate and temperature gradients within the material. The thin-walled vessel experiences the same ambient temperature as a bulk material; however, the freezing rate is dramatically faster for the flow phantom due to the high surface area to volume ratio. This deviation results in altered elastic properties currently unquantified for thin-walled PVA vessels [53]. Under accelerated freeze-thaw cycles, the undefined modification of PVA's mechanical and elastic properties contributes to vessel instability under pressurization. Hence, the anthropomorphic flow phantom cannot currently withstand physiological pressurization and pulsatile flow.

Furthermore, a vessel wall and plaque representation as a single material is an oversimplification of the many plaque components of lipid-rich necrotic core (LRNC), intraplaque hemorrhage (IH), calcium deposits (CD), *etc.* found within a human carotid artery [19]. These structures influence the fluid dynamics, acoustics, and scattering properties of human vessels and plaques; consequently, neglecting to include such structural components is a simplifying assumption to ease anthropomorphic flow phantom fabrication.

4.3 Future Work

To address limitations to phantom fabrication and to validate wall shear stress achieved in the phantom, novel vessel wall materials, increased atherosclerosis plaque resemblance to human carotids, and improved validation simulations will result in anthropomorphic carotid blood flow hemodynamics recapitulated in thin-walled and wall-less anthropomorphic flow phantoms.

To fully encapsulate the geometric, elastic, hemodynamic, and plaque composition of human carotid arteries within an anthropomorphic flow phantom several refinements should be considered. To iterate on the aforementioned limitations, a new vessel material or processing method should be investigated to ensure sufficient wall strength and to establish quantifiable material and acoustic properties. This evolution will allow flow pressurization to simulate physiological hemodynamic conditions and permit tunable modulation of vessel wall elasticity to mimic variability in human arterial

stiffness [54]. Additionally, new mold materials should be studied to prevent high rates of defect production during thin-walled phantom construction. Production of interior vessel wall geometries using 3D printers results in warping of the model as the print cools and material is continually added [55]. Consequentially this distortion frustrates the correct positioning of the inner geometry and increases the rate of defect production. An approach under which greater degrees of precision mold construction is utilized would result in lower defect rates and allow for decreased flow phantom fabrication time.

The Fluid-Structure Interaction (FSI) simulations are currently used as a validating standard to substantiate the carotid flow phantoms. The assumption that the FSI model calculates the true wall shear stress (WSS) is a limitation, as the model may deviate from *in vivo* values. Additionally, the current FSI models cannot efficiently simulate vessel wall motion as the artery expands and contracts throughout the cardiac cycle. Therefore, experimental data gathered under pressurized and pulsatile flow will not correlate with the FSI validation at all time points during the cardiac phases. These limitations elucidate the need for a proper validation standard for phantom WSS.

Future work should seek to allow for independent modulation of plaque characteristics and vessel elasticity and geometry. Additionally, by implanting supplementary materials, plaque structures such as LRNC, IH, and CD can be modeled to emulate human plaque components. Modulating these elements will facilitate the continued development of advanced ultrasound sequences and signal processing for plaque rupture risk assessment. By allowing for flexibility in design, a greater utility can be gleaned from thin-walled and wall-less anthropomorphic flow phantoms.

CHAPTER 5: CONCLUSION

5.1 Closing Remarks

To improve plaque rupture risk assessment for atherosclerosis patients, vessel hemodynamics and plaque composition must be considered. The techniques developed by Anand *et al.* [28], [43] have been shown to effectively perform the aforementioned characterizations using cadaveric carotids and commercially available straight tube flow phantoms to develop the required ultrasound sequences. However, further development will require subjecting current and future techniques to highly variable flow and plaque composition environments. To complete such investigations a method of anthropomorphic flow phantom fabrication has been established using thin-walled and wall-less construction. Through modulation of material properties and vessel geometry, ultrasound sequences can be subjected to conditions mimicking a variety of atherosclerosis plaque progressions. These phantoms will aid in developing techniques used for blood plaque characterization.

REFERENCES

[1] M. P. Lindsay *et al.*, "Global Stroke Fact Sheet 2019." World Stroke Organization.

[2] J. W. Cannon, "Hemorrhagic Shock," *N. Engl. J. Med.*, vol. 378, no. 4, pp. 370–379, Jan. 2018, doi: 10.1056/NEJMra1705649.

[3] S. A. Randolph, "Ischemic Stroke," *Workplace Health Saf.*, vol. 64, no. 9, pp. 444–444, Sep. 2016, doi: 10.1177/2165079916665400.

[4] A. M and Y. KS, "Pathogenesis of Atherosclerosis A Review," *Med. Clin. Rev.*, vol. 2, no. 3:22, Aug. 2016, doi: 10.21767/2471-299X.100031.

[5] H. J. M. M. Mutsaerts *et al.*, "Diastolic Carotid Artery Wall Shear Stress Is Associated With Cerebral Infarcts and Periventricular White Matter Lesions," *Stroke*, vol. 42, no. 12, pp. 3497–3501, Dec. 2011, doi: 10.1161/STROKEAHA.111.614453.

[6] S.-K. Jeong, J.-Y. Lee, and R. S. Rosenson, "Association between Ischemic Stroke and Vascular Shear Stress in the Carotid Artery," *J. Clin. Neurol.*, vol. 10, no. 2, p. 133, 2014, doi: 10.3988/jcn.2014.10.2.133.

[7] W. W. Nichols and M. F. O'Rourke, *McDonald's Blood Flow in Arteries: Theoretical, Experimental and Clinical Principles*, 6th ed. London: Hodder Education, 2011.

[8] Y. A. Çengel and J. M. Cimbala, *Fluid mechanics: fundamentals and applications*. Boston: McGraw-HillHigher Education, 2006.

[9] "Carotid bifurcation atherosclerosis. Quantitative correlation of plaque localization with flow velocity profiles and wall shear stress.," *Circ. Res.*, vol. 53, no. 4, p. 13, 1983.

[10] Y. S. Chatzizisis, A. U. Coskun, M. Jonas, E. R. Edelman, C. L. Feldman, and P. H. Stone, "Role of Endothelial Shear Stress in the Natural History of Coronary Atherosclerosis and Vascular Remodeling," *J. Am. Coll. Cardiol.*, vol. 49, no. 25, pp. 2379–2393, Jun. 2007, doi: 10.1016/j.jacc.2007.02.059.

[11] P. F. Davies, A. Remuzzi, E. J. Gordon, C. F. Dewey, and M. A. Gimbrone, "Turbulent fluid shear stress induces vascular endothelial cell turnover in vitro.," *Proc. Natl. Acad. Sci.*, vol. 83, no. 7, pp. 2114–2117, Apr. 1986, doi: 10.1073/pnas.83.7.2114.

[12] K. Lin *et al.*, "Molecular mechanism of endothelial growth arrest by laminar shear stress," *Proc. Natl. Acad. Sci.*, vol. 97, no. 17, pp. 9385–9389, Aug. 2000, doi: 10.1073/pnas.170282597.

[13] Y.-S. J. Li, J. H. Haga, and S. Chien, "Molecular basis of the effects of shear stress on vascular endothelial cells," *J. Biomech.*, vol. 38, no. 10, pp. 1949–1971, Oct. 2005, doi: 10.1016/j.jbiomech.2004.09.030.

[14] S. Chien, "Molecular and mechanical bases of focal lipid accumulation in arterial wall," *Prog. Biophys. Mol. Biol.*, vol. 83, no. 2, pp. 131–151, Oct. 2003, doi: 10.1016/S0079-6107(03)00053-1.

[15] H. C. Groen *et al.*, "Plaque Rupture in the Carotid Artery Is Localized at the High Shear Stress Region: A Case Report," *Stroke*, vol. 38, no. 8, pp. 2379–2381, Aug. 2007, doi: 10.1161/STROKEAHA.107.484766.

[16] Y. Fukumoto *et al.*, "Localized Elevation of Shear Stress Is Related to Coronary Plaque Rupture," *J. Am. Coll. Cardiol.*, vol. 51, no. 6, pp. 645–650, Feb. 2008, doi: 10.1016/j.jacc.2007.10.030.

[17] D. Tang *et al.*, "Sites of Rupture in Human Atherosclerotic Carotid Plaques Are Associated With High Structural Stresses: An In Vivo MRI-Based 3D Fluid-Structure Interaction Study," *Stroke*, vol. 40, no. 10, pp. 3258–3263, Oct. 2009, doi: 10.1161/STROKEAHA.109.558676.

[18] M. Rafieian-Kopaei, M. Setorki, M. Doudi, A. Baradaran, and H. Nasri, "Atherosclerosis: Process, Indicators, Risk Factors and New Hopes," *Int. J. Prev. Med.*, vol. 5, no. 8, p. 20, 2014.

[19] M. I. Tomey, J. Narula, and J. C. Kovacic, "Advances in the Understanding of Plaque Composition and Treatment Options," *J. Am. Coll. Cardiol.*, vol. 63, no. 16, pp. 1604–1616, Apr. 2014, doi: 10.1016/j.jacc.2014.01.042.

[20] P. K. Shah, "Mechanisms of plaque vulnerability and rupture," *J. Am. Coll. Cardiol.*, vol. 41, no. 4, pp. S15–S22, Feb. 2003, doi: 10.1016/S0735-1097(02)02834-6.

[21] D. Katritsis, L. Kaiktsis, A. Chaniotis, J. Pantos, E. P. Efstathopoulos, and V. Marmarelis, "Wall Shear Stress: Theoretical Considerations and Methods of Measurement," *Prog. Cardiovasc. Dis.*, vol. 49, no. 5, pp. 307–329, Mar. 2007, doi: 10.1016/j.pcad.2006.11.001.

[22] P. J. Brands, A. P. G. Hoeks, L. Hofstra, and R. S. Reneman, "A noninvasive method to estimate wall shear rate using ultrasound," *Ultrasound Med. Biol.*, vol. 21, no. 2, pp. 171–185, Jan. 1995, doi: 10.1016/S0301-5629(94)00111-1.

[23] H. I. Goldsmith and R. Skalak, "Hemodynamics," *Annu. Rev. Fluid Mech.*, vol. 7, no. 1, pp. 213–247, 1975.

[24] C. V. Bourantas *et al.*, "A method for 3D reconstruction of coronary arteries using biplane angiography and intravascular ultrasound images," *Comput. Med. Imaging Graph.*, vol. 29, no. 8, pp. 597–606, Dec. 2005, doi: 10.1016/j.compmedimag.2005.07.001.

[25] R. Stokholm, S. Oyre, S. Ringgaard, H. Flaagoy, W. Paaske, and E. Pedersen, "Determination of Wall Shear Rate in the Human Carotid Artery by Magnetic Resonance Techniques," *Eur. J. Vasc. Endovasc. Surg.*, vol. 20, no. 5, pp. 427–433, Nov. 2000, doi: 10.1053/ejvs.2000.1221.

[26] R. S. Reneman, T. Arts, and A. P. G. Hoeks, "Wall Shear Stress – an Important Determinant of Endothelial Cell Function and Structure – in the Arterial System in vivo," *J. Vasc. Res.*, vol. 43, no. 3, pp. 251–269, 2006, doi: 10.1159/000091648.

[27] P. Yim, K. Demarco, M. A. Castro, and J. Cebral, "Characterization of shear stress on the wall of the carotid artery using magnetic resonance imaging and computational fluid dynamics," *Stud. Health Technol. Inform.*, vol. 113, pp. 412–442, Jan. 2005.

[28] K. S. Anand and C. M. Gallippi, "Multiangle PW Compounding Supports ARFI Variance of Acceleration (VoA) Carotid Plaque Imaging for Integration with Vector Doppler," in *2021 IEEE International Ultrasonics Symposium (IUS)*, Xi'an, China, Sep. 2021, pp. 1–3. doi: 10.1109/IUS52206.2021.9593578.

[29] G. Torres *et al.*, "Delineation of Human Carotid Plaque Features In Vivo by Exploiting Displacement Variance," *IEEE Trans. Ultrason. Ferroelectr. Freq. Control*, vol. 66, no. 3, pp. 481–492, Mar. 2019, doi: 10.1109/TUFFC.2019.2898628.

[30] W. F. Walker and G. E. Trahey, "A fundamental limit on delay estimation using partially correlated speckle signals," *IEEE Trans. Ultrason. Ferroelectr. Freq. Control*, vol. 42, no. 2, pp. 301–308, Mar. 1995, doi: 10.1109/58.365243.

[31] J. V. Soulis *et al.*, "Spatial and phasic oscillation of non-Newtonian wall shear stress in human left coronary artery bifurcation: an insight to atherogenesis," *Coron. Artery Dis.*, vol. 17, no. 4, pp. 351–358, Jun. 2006.

[32] J. Dong, Y. Zhang, and W.-N. Lee, "Walled vessel-mimicking phantom for ultrasound imaging using 3D printing with a water-soluble filament: design principle, fluid-structure interaction (FSI) simulation, and experimental validation," *Phys. Med. Biol.*, vol. 65, no. 8, p. 085006, Apr. 2020, doi: 10.1088/1361-6560/ab7abf.

[33] F. Galluzzo, F. Leonardo, A. Ceruti, L. De Marchi, and C. Corsi, "Design of anthropomorphic atherosclerotic carotid artery flow phantoms for ultrasound images," in *2015 Computing in Cardiology Conference (CinC)*, Nice, Sep. 2015, pp. 721–724. doi: 10.1109/CIC.2015.7411012.

[34] A. J. Y. Chee, C. K. Ho, B. Y. S. Yiu, and A. C. H. Yu, "Walled Carotid Bifurcation Phantoms for Imaging Investigations of Vessel Wall Motion and Blood Flow Dynamics," *IEEE Trans. Ultrason. Ferroelectr. Freq. Control*, vol. 63, no. 11, pp. 1852–1864, Nov. 2016, doi: 10.1109/TUFFC.2016.2591946.

[35] S. R. Sompuram, K. Vani, E. Messana, and S. A. Bogen, "A Molecular Mechanism of Formalin Fixation and Antigen Retrieval," *Am. J. Clin. Pathol.*, vol. 121, no. 2, pp. 190–199, Feb. 2004, doi: 10.1309/BRN7CTX1E84NWWPL.

[36] F. Duboeuf, A. Basarab, H. Liebgott, E. Brusseau, P. Delachartre, and D. Vray, "Investigation of PVA cryogel Young's modulus stability with time, controlled by a simple reliable technique: Investigation of PVA cryogel Young's stability with time," *Med. Phys.*, vol. 36, no. 2, pp. 656–661, Jan. 2009, doi: 10.1118/1.3065031.

[37] Y. Zhang, "Measuring Acoustic Attenuation of Polymer Materials Using Drop Ball Test," p. 121.

[38] E. L. Madsen, J. A. Zagzebski, R. A. Banjavie, and R. E. Jutila, "Tissue mimicking materials for ultrasound phantoms," *Med. Phys.*, vol. 5, no. 5, pp. 391–394, Sep. 1978, doi: 10.1118/1.594483.

[39] K. K. Dakok, M. Z. Matjafri, N. Suardi, A. A. Oglat, and S. E. Nabasu, "A Review of Carotid Artery Phantoms for Doppler Ultrasound Applications," *J. Med. Ultrasound*, vol. 29, no. 3, pp. 157–166, Sep. 2021, doi: 10.4103/JMU.JMU_164_20.

[40] H. M. Loree, B. J. Tobias, L. J. Gibson, R. D. Kamm, D. M. Small, and R. T. Lee, "Mechanical properties of model atherosclerotic lesion lipid pools.," *Arterioscler. Thromb. J. Vasc. Biol.*, vol. 14, no. 2, pp. 230–234, Feb. 1994, doi: 10.1161/01.ATV.14.2.230.

[41] Q. Tate, S.-E. Kim, G. Treiman, D. L. Parker, and J. R. Hadley, "Increased vessel depiction of the carotid bifurcation with a specialized 16-channel phased array coil at 3T," *Magn. Reson. Med.*, vol. 69, no. 5, pp. 1486–1493, 2013, doi: 10.1002/mrm.24380.

[42] J. B. Thomas, L. Jong, J. D. Spence, B. A. Wasserman, B. K. Rutt, and D. A. Steinman, "Anthropometric data for magnetic resonance imaging of the carotid bifurcation," *J. Magn. Reson. Imaging*, vol. 21, no. 6, pp. 845–849, 2005, doi: 10.1002/jmri.20317.

[43] K. Anand, J. Homeister, J. A. Ezzel, G. Torres, and C. M. Gallippi, "Combined ARFI Variance of Acceleration (VoA), Vector Flow, and Wall Shear Stress for Assessing Atherosclerotic Risk: Ex-Vivo Human Cadaveric Results," in *2020 IEEE International Ultrasonics Symposium (IUS)*, Las Vegas, NV, USA, Sep. 2020, pp. 1–4. doi: 10.1109/IUS46767.2020.9251826.

[44] D. M. King, N. J. Hangiandreou, D. J. Tradup, and S. F. Stekel, "Evaluation of a low-cost liquid ultrasound test object for detection of transducer artefacts," *Phys. Med. Biol.*, vol. 55, no. 23, pp. N557–N570, Nov. 2010, doi: 10.1088/0031-9155/55/23/N01.

[45] R. Leibuss *et al.*, "Transcranial Duplex Ultrasonography Measurements Towards Identification of Blood Vessel Conditions: Artificial Cerebral Blood Flow in Pathologies," *Proc. Latv. Acad. Sci. Sect. B Nat. Exact Appl. Sci.*, vol. 76, no. 3, pp. 346–351, Jun. 2022, doi: 10.2478/prolas-2022-0052.

[46] T. J. Czernuszewicz *et al.*, "Performance of acoustic radiation force impulse ultrasound imaging for carotid plaque characterization with histologic validation," *J. Vasc. Surg.*, vol. 66, no. 6, pp. 1749-1757.e3, Dec. 2017, doi: 10.1016/j.jvs.2017.04.043.

[47] R. H. Behler *et al.*, "Acoustic radiation force beam sequence performance for detection and material characterization of atherosclerotic plaques: preclinical, ex vivo results," *IEEE Trans. Ultrason. Ferroelectr. Freq. Control*, vol. 60, no. 12, pp. 2471–2487, Dec. 2013, doi: 10.1109/TUFFC.2013.2847.

[48] E. M. Kolahdouz, A. P. S. Bhalla, B. A. Craven, and B. E. Griffith, "An immersed interface method for discrete surfaces," *J. Comput. Phys.*, vol. 400, p. 108854, Jan. 2020, doi: 10.1016/j.jcp.2019.07.052.

[49] T. L. Szabo, *Diagnostic ultrasound imaging: inside out*. Amsterdam ; Boston: Elsevier Academic Press, 2004.

[50] K. Anand, G. Torres, and C. Gallippi, "Experimental Evaluation of the Impact of Signal Decorrelation on Plane Wave versus Focused ARFI VoA Measurements," in *2020 IEEE International Ultrasonics Symposium (IUS)*, Las Vegas, NV, USA, Sep. 2020, pp. 1–3. doi: 10.1109/IUS46767.2020.9251598.

[51] J. Fromageau, E. Brusseau, D. Vray, G. Gimenez, and P. Delachartre, "Characterization of PVA cryogel for intravascular ultrasound elasticity imaging," *IEEE Trans. Ultrason. Ferroelectr. Freq. Control*, vol. 50, no. 10, pp. 1318–1324, Oct. 2003, doi: 10.1109/TUFFC.2003.1244748.

[52] W. M. Rohsenow, J. P. Hartnett, and E. N. Ganić, Eds., *Handbook of heat transfer fundamentals*, 2nd ed. New York: McGraw-Hill, 1985.

[53] J. Fromageau, J.-L. Gennisson, C. Schmitt, R. L. Maurice, R. Mongrain, and G. Cloutier, "Estimation of polyvinyl alcohol cryogel mechanical properties with four ultrasound elastography methods and comparison with gold standard testings," *IEEE Trans. Ultrason. Ferroelectr. Freq. Control*, vol. 54, no. 3, pp. 498–509, Mar. 2007, doi: 10.1109/TUFFC.2007.273.

[54] Y. Lu *et al.*, "Trajectories of Age-Related Arterial Stiffness in Chinese Men and Women," *J. Am. Coll. Cardiol.*, vol. 75, no. 8, pp. 870–880, Mar. 2020, doi: 10.1016/j.jacc.2019.12.039.

[55] J. Ramian, J. Ramian, and D. Dziob, "Thermal Deformations of Thermoplast during 3D Printing: Warping in the Case of ABS," *Materials*, vol. 14, no. 22, Art. no. 22, Jan. 2021, doi: 10.3390/ma14227070.